

When does the elastic regime begin in viscoelastic pinch-off?

A. Gaillard^a, M. A. Herrada^b, A. Deblais^a, C. van Poelgeest^a, L. Laruelle^a, J. Eggers^c, D. Bonn^a

^a*Van der Waals-Zeeman Institute, University of Amsterdam, Science Park 904, Amsterdam, Netherlands*

^b*Depto. de Mecánica de Fluidos e Ingeniería Aeroespacial, Universidad de Sevilla, Sevilla, E-41092, Spain*

^c*School of Mathematics, University of Bristol, University Walk, Bristol, BS8 1 TW, United Kingdom*

Abstract

In this experimental and numerical study, we revisit the question of the onset of the elastic regime in viscoelastic pinch-off. This is relevant for all modern filament thinning techniques which aim at measuring the extensional properties of low-viscosity polymer solutions such as the Slow Retraction Method (SRM) in Capillary Breakup Extensional Rheometry (CaBER) as well as the dripping method where a drop detaches from a nozzle. In these techniques, a stable liquid bridge is slowly brought to its stability threshold where capillary-driven thinning starts, slowing down dramatically at a critical radius h_1 marking the onset of the elastic regime where the bridge becomes a filament with elasto-capillary thinning dynamics. While a theoretical scaling for this transition radius exists for the classical step-strain CaBER protocol, where polymer chains stretch without relaxing during the fast plate separation, we show that it is not necessarily valid for a slow protocol such as in SRM since polymer chains only start stretching (beyond their equilibrium coiled configuration) when the bridge thinning rate becomes comparable to the inverse of their relaxation time. We derive a universal scaling for h_1 valid for both low and high-viscosity polymer solution which is validated by both CaBER (SRM) experiments with different polymer solutions, plate diameters and sample volumes and by numerical simulations using the FENE-P model.

Keywords: Viscoelasticity, Filament, Pinch-off

1. Introduction

The elasticity of a polymer solution can be probed by stretching a drop between one's thumb and index finger, resulting in the formation of a filament with a persistence time

*Corresponding author

Email address: antoineogaillard@gmail.com (A. Gaillard)

which is linked to the relaxation time of the solution. Such filaments are observable in many industrial free-surface flows such as spraying [1–3] and inkjet printing [4, 5], where long polymer molecules can be added to a Newtonian solvent to achieve a specific flow property, as well as in ejecta produced when coughing and sneezing [6, 7]. The capillary-driven thinning dynamics of these filaments is the basis of numerous rheometry techniques dedicated to low-viscosity fluids, for which other techniques such as Meissner’s RME (Rheometric Melt Elongation rheometer) and FiSER (Filament Stretching Extensional Rheometer) are not applicable. These techniques include Capillary Breakup Extensional Rheometry (CaBER) where a droplet is confined between two plates which are separated beyond the the range of stable liquid bridges [8–10], the dripping technique where a droplet detaches from a nozzle [11–13] and Dripping-onto-Substrate (DoS) where a solid substrate is brought into contact with a drop hanging steadily from a nozzle [14]. All these techniques aim at creating a viscoelastic filament by triggering the pinching of a liquid column via the Rayleigh-Plateau instability.

Viscoelastic filaments are found to thin exponentially over time for a wide range of polymer-solvent systems and polymer concentrations (dilute and semi-dilute), consistent with the Oldroyd-B model which predicts

$$h = h_1 \exp\left(-\frac{t - t_1}{3\tau}\right), \quad (1)$$

where h is the (minimum) filament radius and τ the relaxation time of the polymer solution, the longest one for a multimode model [9, 15]. This regime corresponds to an elasto-capillary balance where the elastic stress arising from the stretching of polymer chains balances the driving capillary pressure. Experimentally, starting from an equilibrium situations where polymers are relaxed (no pre-stress), this elastic regime can only be observed once polymers have been sufficiently stretched to overcome inertia and/or viscosity, which occurs at a time t_1 and at a filament radius $h_1 = h(t_1)$ marked by a sudden deceleration of the thinning dynamics.

The amount of stretching of polymer chains at times $t < t_1$ is set by the strength of the extensional flow in the pinching region. In the limit case where the thinning dynamics at times $t < t_1$ (before elasticity balances capillarity) is much faster than the solution’s relaxation time, i.e., where polymer chains deform by the same amount as the surrounding solvent itself without relaxing, Clasen et al. [16] showed that the Oldroyd-B model leads to

$$h_1 = \left(\frac{Gh_0^4}{2\gamma}\right)^{1/3}, \quad (2)$$

where γ is the surface tension, G the elastic modulus and h_0 the radius of the ‘initial’ liquid column before the onset of capillary thinning, i.e., when the fluid is still at rest. This formula

was first derived by Bazilevsky et al. [8] and differs by a factor $2^{1/3}$ from the formula proposed by Entov and Hinch [15] who did not treat the tension in the filament properly.

This ‘relaxation-free’ scenario leading to equation 2 corresponds to the step-strain CaBER protocol where the plates are separated so fast that polymer chains stretch without having time to relax as the liquid bridge, connecting the two plates, stretches axially. In this step-strain protocol, the plates are separated exponentially over time to create an extensional flow with a constant extension rate $\dot{\epsilon}_0$ which, to ensure that polymer relaxation is negligible, must be larger than the coil-stretch transition value $1/2\tau$ [17]. This corresponds to Weissenberg number $Wi_0 = \dot{\epsilon}_0\tau > 1/2$. Once the plates have reached their final separation distance L_f , the unstable liquid bridge between the two plates continues to thin, this time under the action of capillarity, until the elastic regime starts at a bridge / filament (minimum) radius h_1 . Miller et al [17] showed that, consistent with equation 2, h_1 does not depend on L_f for polymer solutions. We are however unaware of experimental studies where h_1 was reported and tested against equation 2 for different plate diameters and initial gaps, which set the radius h_0 of the initial (unloaded) fluid sample, or for different polymer solutions.

This step-strain CaBER protocol is however not recommended for low-viscosity polymer solutions since a fast plate separation leads to inertio-capillary oscillations of the end-drops which hinder the measurement of the relaxation time [18]. Alternative protocols consist in reaching the threshold of the Rayleigh-Plateau instability slowly, e.g. by separating the plates at a constant low velocity in CaBER (Slow Retraction Method or SRM) [19]. In that case, the initially stable liquid bridge connecting the two end-plates becomes unstable at a critical plate separation distance, corresponding to a minimum bridge radius h_0 , and thins further under the action of capillarity. This is similar to the dripping method where the bridge connecting a droplet to a nozzle, from which liquid is infused at a low flow rate, becomes unstable at a critical droplet weight [13].

In such slow protocols, equation 2 may not be valid if the time taken by the bridge to thin from its initial (minimum) radius h_0 to the radius h_1 (marking the onset of the elastic regime) is larger than the liquid’s relaxation time τ , as was already noticed by Bazilevsky et al. [8]. In that case, polymer chains may indeed remain in a coiled state for a significant time, only starting to stretch when the bridge’s thinning rate becomes comparable to $1/\tau$. This led Campo-Deaño & Clasen [19] to derive an alternative formula for h_1 for their slow retraction CaBER method which, to our knowledge, has never been tested experimentally. In this formula, h_1 is independent of h_0 , in sharp contrast with equation 2 which predicts $h_1 \propto h_0^{4/3}$. In a more recent experimental work from Rajesh et al. [13], the authors proposed an empirical scaling $h_1 \propto R_n^{0.66}$ in dripping experiments with low-viscosity polymer solutions where R_n is the nozzle radius, but they did not provide a theoretical explanation for their findings.

In such slow protocols, equation 2 is only expected to be valid if the time taken by the

liquid bridge to thin from h_0 to h_1 is much shorter than the liquid's relaxation time, in which case polymer chains stretch without having time to relax. This time is expected to scale as the characteristic time scale of the capillary-driven bridge thinning dynamics derived from linear stability theory, namely, the Rayleigh (inertio-capillary) time scale [20]

$$\tau_R = (\rho h_0^3 / \gamma)^{1/2}, \quad (3)$$

or the visco-capillary time scale

$$\tau_{\text{visc}} = \eta_0 h_0 / \gamma, \quad (4)$$

depending on the Ohnesorge number

$$Oh = \frac{\eta_0}{\sqrt{\rho \gamma h_0}} = \frac{\tau_{\text{visc}}}{\tau_R}, \quad (5)$$

where ρ and η_0 are the liquid density and total (zero-shear) viscosity, respectively. In other words, if we define a Deborah number

$$De = \tau / \tau_R \quad (6)$$

based on the Rayleigh time scale, equation 2 is expected to be valid for $De \gg 1$ in the inviscid case ($Oh \ll 1$) and for $De/Oh = \tau/\tau_{\text{visc}} \gg 1$ in the viscous case ($Oh \gg 1$), which is the limit considered in most analytical studies [16].

In this study, we aim to expand our current understanding of the transition radius h_1 (marking the onset of the elastic regime) to cases where polymer relaxation is not negligible during the capillary driven thinning of the liquid bridge. This discussion follows up on our previous paper where h_1 was observed to increase linearly with h_0 for different liquids for a slow plate separation CaBER protocol [21], a scaling which differs from the $h_1 \propto h_0^{4/3}$ prediction of equation 2. Materials and methods are presented in §2 and experimental results are presented in §3. Theoretical expressions of h_1 are derived and tested experimentally and numerically using the Oldroyd-B model in §4 and the FENE-P model in §5.

2. Materials and methods

The liquids, their shear rheology and the setup used in experiments are presented in §2.1 and §2.2 and §2.3, respectively, while the equations and numerical methods used in simulations are presented in §2.4.

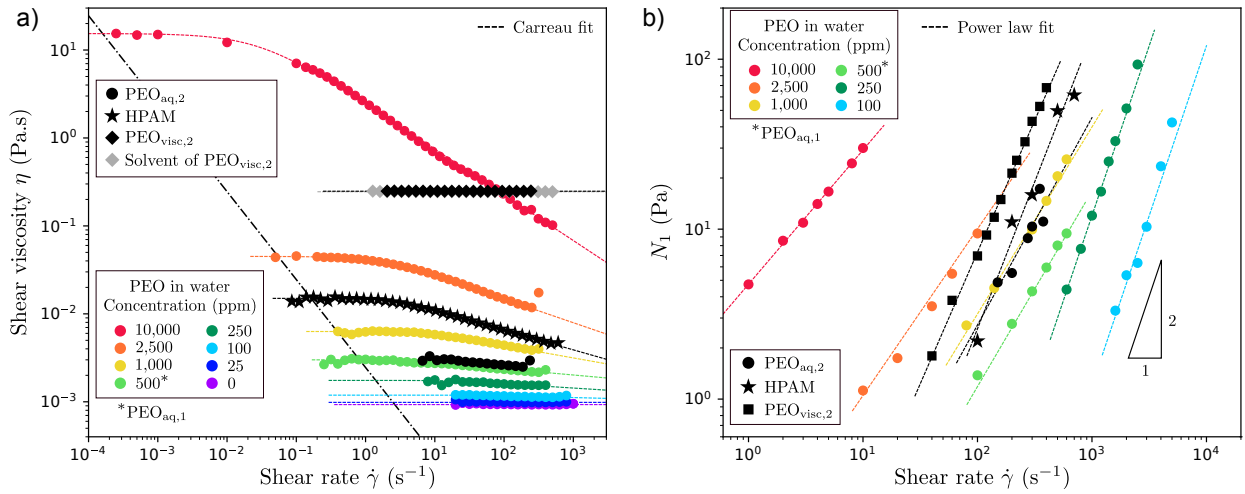


Figure 1: (a) Shear viscosity η and (b) first normal stress difference N_1 of the different polymer solutions against the shear rate $\dot{\gamma}$.

2.1. Liquids

Three of the polymer solutions used in the present study are the same as in our previous paper [21] which have comparable ‘relaxation times’ or, more precisely, comparable filament thinning rates. Two of them are solutions of poly(ethylene oxide) (PEO) of molecular weight $M_w = 4 \times 10^6$ g/mol (PEO-4M), one in water with concentration 500 ppm, referred to as PEO_{aq} , and one in a ~ 260 times more viscous solvent with concentration 25 ppm, referred to as PEO_{visc} , and the third one is a 1000 ppm solution of poly(acrylamide/sodium acrylate) (HPAM) [70:30] of molecular weight $M_w = 18 \times 10^6$ g/mol in water with 1 wt% NaCl to screen electrostatic interactions and make the chain flexible instead of semi-rigid. Both polymers were provided by Polysciences (ref. 04030-500 for PEO and 18522-100 for HPAM). The solvent of the PEO_{visc} solution is a Newtonian 30 wt% aqueous solution of poly(ethylene glycol) (PEG) with molecular weight 20,000 g/mol (PEG-20K). After slowly injecting the polymer powder to a vortex generated by a magnetic stirrer, solutions were homogenised using a mechanical stirrer at low rotation speed for about 16 hours. For the PEO_{visc} solution, PEG was added after mixing PEO with water. Additional solutions of PEO-4M in water were prepared from dilution of a 10,000 ppm stock solution with concentrations ranging between 5 and 10,000 ppm to investigate the influence of polymer concentration.

2.2. Shear rheology

The shear viscosity η and first normal stress difference N_1 of polymer solutions were measured at the temperature of CaBER experiments, typically 20°C, with a MRC-302 rheometer

c (ppm)	γ (mN/m)	c/c^*	η_0 (mPa s)	η_p (mPa s)	n	$1/\dot{\gamma}_c$ (s)	α_1	Ψ_1 (Pa s $^{\alpha_1}$)
5	72.0	0.019	0.93	0.013	1	–	–	–
10	72.0	0.037	0.940	0.02	1	–	–	–
25	63.4	0.093	0.985	0.065	1	–	–	–
50	62.8	0.19	1.04	0.12	1	–	–	–
100	63.0	0.37	1.19	0.27	0.98	0.023	2	1.2×10^{-6}
250	63.0	0.93	1.75	0.83	0.95	0.054	2	1.2×10^{-5}
500	62.5	1.9	3.00	2.08	0.95	0.12	1.15	5.9×10^{-3}
1000	62.5	3.7	6.3	5.38	0.86	0.14	1.10	2.0×10^{-2}
2500	62.5	9.3	45	44	0.73	0.62	0.98	1.1×10^{-1}
10000	62.3	37	15400	15400	0.48	34	0.79	4.7×10^0

Table 1: Concentration c , reduced concentration c/c^* , surface tension γ and shear rheological properties (from equations 7 and 8) of aqueous PEO-4M solutions prepared from dilution of the same 10,000 ppm stock solution. $\eta_p = \eta_0 - \eta_s$ is the polymer contribution to the shear viscosity. The density and solvent viscosity are $\rho = 998 \text{ kg/m}^3$ and $\eta_s = 0.92 \text{ mPa s}$. The 500ppm solution in this table is referred to as PEO_{aq,1} in the text. For the 5 ppm solution, η_0 is too close to η_s to estimate η_p and we therefore use $\eta_p = \eta_s[\eta]c$ with the intrinsic viscosity $[\eta]$ extracted from the linear fit of $\eta_p(c)$ for $c < c^*$.

from Anton Paar equipped with a cone plate geometry (diameter 50 mm, angle 1° and truncation gap $53 \mu\text{m}$) and are shown in figure 1. To measure N_1 , we follow a step-by-step protocol similar to Casanellas et al. [22] in order to circumvent the instrumental drift of the normal force. This protocol consists in applying steps of constant shear rate followed by steps of zero shear and subtracting the two raw N_1 plateau values. The contribution of inertia to the normal force is corrected for by the rheometer [23]. We find that the PEO_{visc} solution is a Boger fluid with a constant shear viscosity while the HPAM solution is shear-thinning, as well as the aqueous PEO solutions when concentrations are larger than 250 ppm. For shear-thinning solutions, the shear viscosity is fitted with the Carreau-Yasuda formula

$$\eta(\dot{\gamma}) = \eta_0(1 + (\dot{\gamma}/\dot{\gamma}_c)^{a_1})^{(n-1)/a_1}, \quad (7)$$

where η_0 is the zero-shear viscosity, n is the shear-thinning exponent and $\dot{\gamma}_c$ is the shear rate marking the onset of shear thinning, a_1 (typically 2) encoding the sharpness of the transition towards the shear thinning regime. The polymer contribution to the shear viscosity $\eta_p = \eta_0 - \eta_s$ increases linearly with polymer concentration c in the dilute regime and follows $\eta_p = \eta_s[\eta]c$ where, for the PEO solutions in water, we find an intrinsic viscosity $[\eta] = 2.87 \text{ m}^3/\text{kg}$. Using the expression of Graessley [24], gives a critical overlap concentration $c^* = 0.77/[\eta] = 0.268 \text{ kg/m}^3$ (268 ppm), consistent with the onset of shear-thinning expected at $c > c^*$. For the PEO_{visc} solution, where only one concentration (25 ppm) was tested, assuming that the solution is dilute to calculate $[\eta]$ and c^* using the same formulas leads

Name	ρ (kg/m ³)	γ (mN/m)	η_s (mPa s)	c (ppm)	c/c^*	η_0 (mPa s)	η_p (mPa s)	n	$1/\dot{\gamma}_c$ (ms)	α_1	Ψ_1 (Pa s ^{α_1})	τ_m (ms)
PEO _{aq,2}	998	62.5	0.92	500	1.9	3.3	2.08	0.93	120	1.2	9.9×10^{-3}	240
PEO _{visc,2}	1048	56.0	245	25	0.018	248	3.3	1	–	1.6	5.8×10^{-3}	110
HPAM	998	72.0	0.92	1000	–	15	14	0.78	410	1.7	9.0×10^{-3}	100

Table 2: Properties of the polymer solutions used for plate diameters $2R_0$ up to 25 mm in CaBER measurements. ρ is the density and γ is the surface tension. See caption of table 1 for the definition of the shear properties. τ_m is the maximum CaBER relaxation time measured for the largest plates, see figure 4(a). The PEO_{visc,1} and PEO_{visc,2} solutions have the same shear viscosity to within less than 5 %.

to a larger critical overlap concentration $c^* = 1400$ ppm, probably due to differences in polymer-solvent interactions (PEO in water vs. PEO in PEG solution). The first normal stress difference is fitted by a power law

$$N_1 = \Psi_1 \dot{\gamma}^{\alpha_1}, \quad (8)$$

where we find $\alpha_1 = 2$ below c^* and $\alpha_1 < 2$ above c^* for aqueous PEO solutions, and $\alpha_1 < 2$ for the PEO_{visc} and HPAM solutions. All fitting parameters are reported in table 1 for the PEO solutions of different concentrations in water, and in table 2 for the PEO_{aq}, PEO_{visc} and HPAM solutions. We also report the density ρ and surface tension γ measured with a pendant drop method and, when known, the ratio c/c^* .

We must mention here that two different PEO_{aq} solutions and two different PEO_{visc} solutions have been used in this study, with differences in rheological properties in each case, caused by slightly different preparation protocols for a given recipe (e.g., a slightly different agitation time). The PEO_{aq,1} solution is prepared from dilution of the same stock solution as the other aqueous PEO solutions in table 1. The PEO_{aq,2} solution featured in table 2 exhibits a 10% larger shear viscosity and about 2.5 times larger values of N_1 , as shown in figure 1. The PEO_{visc,1} and PEO_{visc,2} solutions have the same shear viscosity to within less than 5 % and only the latter one is presented in figure 1 and in table 2. As explained in §2.3, the PEO_{aq,1} and PEO_{visc,1} solutions were tested with (CaBER) plate diameters less than 7 mm, varying the (non-dimensional) drop volume for each plate, whereas the PEO_{aq,2} and PEO_{visc,2} solutions were used for plate diameters up to 25 mm with a single (non-dimensional) drop volume for each plate.

2.3. Experimental setup and slow-stepwise CaBER protocol

The CaBER setup and slow-stepwise plate separation protocol described here are the same as in our previous paper [21]. A droplet of volume V is placed on a horizontal plate of radius R_0 and the motor-controlled top plate of same radius is first moved down until

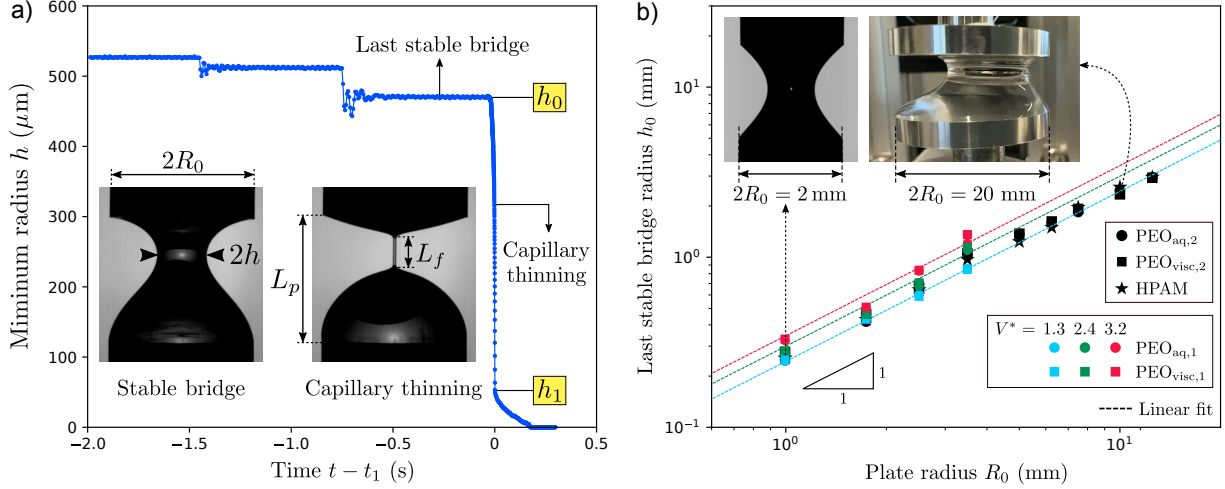


Figure 2: (a) Time evolution of the minimum bridge / filament radius h in our slow stepwise plate separation protocol for the $\text{PEO}_{\text{aq},1}$ solution for plate diameter $2R_0 = 3.5$ mm and a droplet volume $V^* = V/R_0^3 \approx 2.4$. Inertio-capillary oscillations are visible after each step. Inset images correspond to a stable liquid bridge (left) and to a thinning filament (right) of the same liquid with $2R_0 = 7$ mm and $V^* \approx 2.4$. (b) Last stable bridge radius h_0 against the plate radius R_0 for $2R_0$ between 2 and 7 mm and, for each plate, $V^* \approx 1.3, 2.4$ and 3.2 for the $\text{PEO}_{\text{aq},1}$ and $\text{PEO}_{\text{visc},1}$ solutions, and for $2R_0$ between 2 and 25 mm and an single volume ($V^* \approx 2.4$ for the smallest plates and 0.88 for the largest plates) for the $\text{PEO}_{\text{aq},2}$ and $\text{PEO}_{\text{visc},2}$ and HPAM solutions. Inset images correspond to stable liquid bridges ($h \geq h_0$) for $2R_0 = 2$ mm (left, $\text{PEO}_{\text{aq},1}$ solution with $V^* \approx 2.4$) and $2R_0 = 20$ mm (right, HPAM solution with $V^* \approx 1.0$).

it is fully wetted by the liquid, i.e., until the liquid bridge between the plates has a quasi cylindrical shape. The top plate is then moved up slowly (at about 0.5 mm/s) and stopped at a plate separation distance L_p where the liquid bridge is still stable, like in the left inset image of figure 2(a), but close to the bridge instability threshold. Then, instead of moving the top plate at a constant (lower) velocity, i.e. like in SRM [19], we move it by $10 \mu\text{m}$ L_p -increment steps, waiting about one second between each step (longer than the solution's relaxation time), which is long enough to ensure that polymers are at equilibrium (no pre-stress) before each new step. At a certain step, the bridge becomes unstable and collapses under the action of surface tension, transiently leading to the formation of a nearly cylindrical filament which is the signature of viscoelastic pinch-off, as shown in the right inset image of figure 2(a). We stop moving the top plate once capillary-driven thinning starts.

The process is recorded by a high-magnification objective mounted on a high-speed camera (Phantom TMX 7510) and images are analysed by a Python code. A typical time-evolution of the minimum bridge / filament radius, labelled ' h_{min} ' by many authors but simply referred to as h in the rest of the paper, is shown in figure 2(a). The purpose of this step-by-step plate separation protocol is to extract the value of the last stable bridge radius h_0 which, since steps

are small, can be considered as the initial bridge radius at the onset of capillary thinning. Our image resolution is up to 1 pixel per micrometer for the smallest drops, corresponding to the smallest plates, and our time resolution is 15,000 images per second to capture the fast bridge collapse from radius h_0 to the radius h_1 marking the onset of the elastic regime, see figure 2(a).

The critical aspect ratio $\Lambda = L_p/(2R_0)$ at which the liquid bridge becomes unstable depends on the liquid volume V and on the Bond number $Bo = \rho g R_0^2 / \gamma$, where g is the gravitational acceleration [25]. In our experiments, we vary the plate diameter $2R_0$, between 2 and 25 mm, as well as the non-dimensional droplet volume

$$V^* = V/R_0^3. \quad (9)$$

As shown in figure 2(b), the last stable bridge radius increases fairly linearly with the plate radius, i.e. $h_0 \propto R_0$ with a prefactor which increases with V^* , with no strong dependence on the liquid used since they all have comparable surface tensions. Typically, h_0/R_0 ranges between 0.24 and 0.35 for $V^* \approx 1.3$ and 3.2, respectively.

The aluminium plates are plasma-treated before each measurement to increase their hydrophilicity and hence prevent dewetting of the top plate. However, dewetting could not be avoided for plate diameters $2R_0 \geq 10$ mm, as shown by the right inset image of figure 2(b) showing a stable liquid bridge ($h \geq h_0$) where the top end-drop does not cover the top plate fully for $2R_0 = 20$ mm. Perhaps surprisingly, h_0 does not saturate at $2R_0 \geq 10$ mm in spite of this lack of full coverage, see figure 2(b). For such large plates, the top end-drop is not necessarily at the centre of the the top plate since the two plates are not perfectly parallel. Note that because of the plasma treatment, there is always a thin film covering the top plate.

All experiments are carried out at a high relative humidity ($> 80\%$) ensured by placing the CaBER setup in a box with wet paper tissues. We checked that repeating an experiment several times over the course of 10 minutes does not lead to any monotonic increase or decrease of the filament thinning rate ($1/3\tau_e$, see §3) over time in the exponential part of the elastic regime, beyond small variations of less than 5%, suggesting that both evaporation and polymer degradation (which may occur during bridge / filament thinning) are negligible.

2.4. Equations and numerical methods

The numerical simulations discussed in §4 and §5 are performed using the FENE-P model which aims to describe polymer stretching as well as the finite extensibility of polymer molecules. We consider a cylindrical axisymmetric (r, z) coordinate system aligned with the vertical axis of the liquid bridge. In the simulations, we integrate the mass and momentum conservation equations of general form

$$\nabla \cdot \mathbf{v} = 0, \quad (10)$$

$$\rho \frac{D\mathbf{v}}{Dt} = -\nabla p + \nabla \cdot \boldsymbol{\sigma}, \quad (11)$$

where ρ , $\mathbf{v} = v_r(r, z, t)\mathbf{e}_r + v_z(r, z, t)\mathbf{e}_z$, and $p(r, z, t)$ are the density, velocity and (reduced) pressure field (accounting for gravity), respectively, and D/Dt is the material derivative. These equations are completed with the constitutive relationships for the stress tensor $\boldsymbol{\sigma} = \boldsymbol{\sigma}_s + \boldsymbol{\sigma}_p$, where

$$\boldsymbol{\sigma}_s = \eta_s (\nabla \mathbf{v} + (\nabla \mathbf{v})^T) \quad (12)$$

is the contribution of the solvent of viscosity η_s and where $\boldsymbol{\sigma}_p$ is the polymer contribution. In the FENE-P model [26], this contribution is calculated as

$$\boldsymbol{\sigma}_p = \frac{\eta_p}{\tau} (f\mathbf{A} - \mathbf{I}), \quad f = \frac{1}{1 - \text{tr}(\mathbf{A})/L^2}, \quad (13)$$

where η_p is the polymer contribution to the zero-shear viscosity $\eta_0 = \eta_s + \eta_p$, τ is the relaxation time and L^2 is the finite extensibility limit, \mathbf{I} being the identity matrix. The conformation tensor \mathbf{A} is calculated from the nonlinear relaxation law

$$\frac{D\mathbf{A}}{Dt} - [(\nabla \mathbf{v})^T \cdot \mathbf{A} + \mathbf{A} \cdot \nabla \mathbf{v}] = -\frac{1}{\tau} (f\mathbf{A} - \mathbf{I}). \quad (14)$$

The free surface location is defined by the equation $r = h(z, t)$. The boundary conditions at that surface are:

$$\frac{\partial h}{\partial t} + h_z w - u = 0, \quad (15)$$

$$-p + gz - \frac{hh_{zz} - 1 - h_z^2}{h(1 + h_z^2)^{3/2}} + \mathbf{n} \cdot \boldsymbol{\sigma} \cdot \mathbf{n} = 0, \quad (16)$$

$$\mathbf{t} \cdot \boldsymbol{\sigma} \cdot \mathbf{n} = 0, \quad (17)$$

where $h_z \equiv dh/dz$, $h_{zz} \equiv d^2h/dz^2$, g is the gravitational acceleration, \mathbf{n} is the unit outward normal vector and \mathbf{t} is the unit vector tangential to the free surface meridians. Equation (15) is the kinematic compatibility condition, while equations (16) and (17) express the balance of normal and tangential stresses respectively. The anchorage condition $h = R_0$ is set at $z = 0$ and $z = L_p$ where L_p is the plate separation distance. The nonslip boundary condition is imposed at the solid surfaces in contact with the liquid. The volume V of the initial configuration is prescribed (and conserved), namely,

$$\pi \int_0^L h^2 dz = V. \quad (18)$$

We start the simulation from liquid bridge at equilibrium with a plate separation distance L_p just below (very close to) the critical one. The breakup process is triggered by applying a very small gravitational force perturbation. We note h_0 the minimum radius of the (stable) liquid bridge just before the perturbation is applied, which is conceptually identical to the last stable bridge radius described in §2.3 for a slow stepwise plate separation protocol.

A numerical simulation is fully determined by five quantities: the Ohnesorge number, the Deborah number, the non-dimensional droplet volume $V^* = V/R_0^3$, the finite extensibility parameter L^2 and the viscosity ratio

$$S = \eta_s/\eta_0. \tag{19}$$

While equations are non-dimensionalised using R_0 and $\sqrt{\rho R_0^3/\gamma}$ as the characteristic length and time scales, we only refer in §4 and §5 to values involving h_0 since, as we will show in §3.1, it is h_0 (not R_0) which is the most relevant length scale of the problem. In particular, we refer to the Rayleigh and viscous time scales and Ohnesorge and Deborah numbers defined in equations 3 to 6.

Simulations are performed in the absence of gravity where the threshold of the Rayleigh-Plateau instability, and therefore the shape of the initial bridge of minimum radius h_0 from which simulations start, is solely determined by V^* . In §4 and §5, instead of referring to V^* , we refer to the value of h_0/R_0 since, in experiments, h_0/R_0 is not only set by V^* but also by the Bond number. We recall that, in experiments, h_0/R_0 ranges between 0.24 and 0.35 for $V^* \approx 1.3$ and 3.2, respectively, see figure 2(b).

The model was solved with a variation of the method described in [27]. The physical domain occupied by the liquid is mapped onto a rectangular domain through a coordinate transformation. Each variable and its spatial and temporal derivatives appearing in the transformed equations were written as a single symbolic vector. Then, we used a symbolic toolbox to calculate the analytical Jacobians of all the equations with respect to the symbolic vector. Using these analytical Jacobians, we generated functions that could be evaluated in the iterations at each point of the discretised numerical domains.

The transformed spatial domain is discretised using $n_\eta = 11$ Chebyshev spectral collocation points in the transformed radial direction η of the domain. We used $n_\xi = 501$ equally spaced collocation points in the transformed axial direction ξ . The axial direction was discretised using second finite differences. Second-order backward finite differences were used to discretise the time domain. We used an automatic variable time step based on the norm of the difference between the solution calculated with a first-order approximation and that obtained from the second-order procedure. The nonlinear system of discretised equations was solved at each time step using the Newton method. The method is fully implicit.

3. Experimental results

In this experimental section, we investigate the role of the plate radius and sample volume in §3.1 and of the polymer concentration in §3.2 on the pinch-off dynamics.

3.1. Influence of the plate radius and drop volume

Image sequences of the pinch-off dynamics are shown in figures 3(a) and 3(b) for the $\text{PEO}_{\text{aq},1}$ (500 ppm PEO-4M in water) solution and the $\text{PEO}_{\text{visc},1}$ (25 ppm PEO-4M in a ~ 260 more viscous solvent) solution, respectively, illustrating the transition from a bridge shape in the Newtonian regime to a filament shape in the elastic regime. For the $\text{PEO}_{\text{aq},1}$ solution, the filament is initially cylindrical until localised pinching is observed near one of the end drops (see frame 6 in figure 3(a)), followed by its destabilisation into a succession of beads connected by thin filaments (which are below our spatial resolution), a phenomenon usually referred to as “blistering” instability [28–31] (see frame 7 and 8). For the $\text{PEO}_{\text{visc},1}$ solution, local pinching occurs very close to breakup and no blistering is observed. In this paper, we refer to the minimum bridge / filament radius h which therefore corresponds to the pinched region if localised pinching occurs. On another note, inertio-capillary oscillations of the top and bottom end drop lead to oscillations of the filament length for the $\text{PEO}_{\text{aq},1}$ solution (see frames 3 to 6 in figure 3(a)). These oscillations are absent for the $\text{PEO}_{\text{visc},1}$ solution due to viscous damping. Note that oscillations do not lead to significant oscillations of the filament radius, implying that when the length of the filament increases, new filament is being created from the liquid in the end drops.

Time evolutions of the minimum bridge / filament radius h are shown in figures 3(c-f) for four plate diameters between 2 and 7 mm and a fixed non-dimensional drop volume $V^* \approx 2.4$ for the $\text{PEO}_{\text{aq},1}$ solution (figures 3(c) and 3(d)) and the $\text{PEO}_{\text{visc},1}$ solution (figures 3(e) and 3(f)) in semi-log (figures 3(c) and 3(e)) and lin-lin (figures 3(d) and 3(f)), the latter focusing on the transition to the elastic regime. The smaller data points correspond to the solvent alone for three of the same plate diameters and, in each case, the same V^* (to within experimental reproducibility). The time reference t_c corresponds to the critical time at which the bridge of solvent alone breaks up. For polymer solutions, since t_c can not be determined, curves are shifted along the time axis until overlapping their corresponding solvent curves. The good overlap between polymer solutions and their solvent at all times $t < t_1$ (before the transition to the elastic regime) confirms that polymers do not affect the pinch-off dynamics in the (hence rightfully called) Newtonian regime. For the $\text{PEO}_{\text{visc},1}$ solution where, as is about to be discussed, capillarity is balanced by viscosity in the Newtonian regime, this solution-solvent overlap is consistent with the low polymer contribution to the total shear viscosity ($\eta_p/\eta_0 = 0.013$). The least good solution-solvent overlaps are explained by experimental differences in V^* .

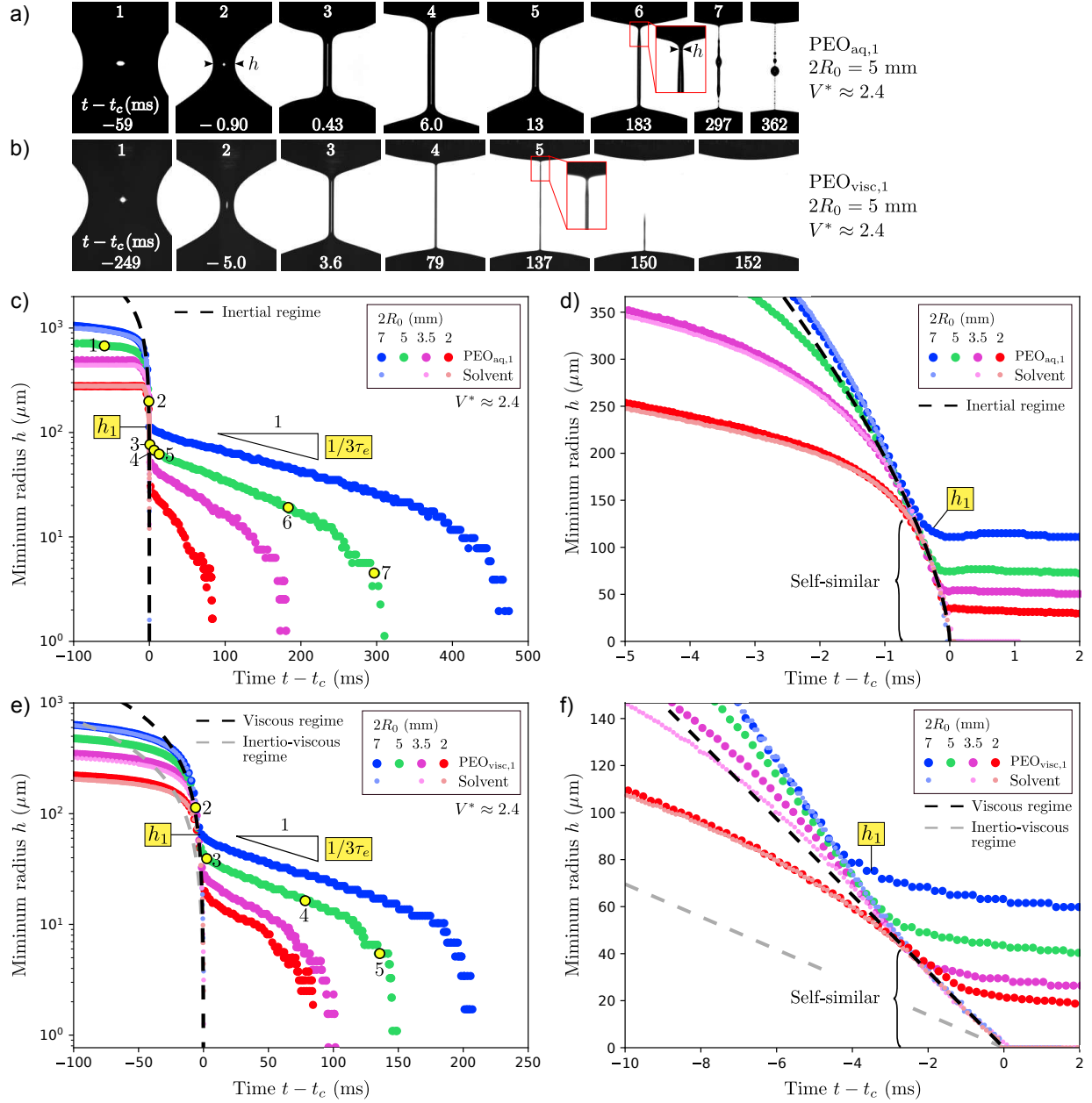


Figure 3: (a,b) Image sequences of the bridge / filament for the PEO_{aq,1} (a) and PEO_{visc,1} (b) solutions tested with plate diameter $2R_0 = 5$ mm and droplet volume $V^* \approx 2.4$. (c-f) Time evolution of the minimum bridge / filament radius h in semi-log (c,e) and lin-lin (d,f), for plate diameters $2R_0$ between 2 and 7 mm and fixed $V^* \approx 2.4$, for the PEO_{aq,1} (c,d) and PEO_{visc,1} (e,f) solutions and for their respective solvents (smaller data points), compared with equations 20 and 21 where t_c is the solvent breakup time. Times with labels 1-7 and 2-5 in panels (c) and (e) for $2R_0 = 5$ mm correspond to the snapshots in panels (a) and (b).

All curves corresponding to Newtonian solvents in figure 3(d,f) overlap close to breakup, indicating a self-similar thinning regime where the information about initial condition, set by R_0 and V^* , is forgotten. Such overlap is also observed for droplets of different volumes for a given plate radius. For the water solvent in figure 3(d), the self-similar regime is well captured by the inertio-capillary thinning law

$$h = A \left(\frac{\gamma}{\rho} \right)^{1/3} (t_c - t)^{2/3}, \quad (20)$$

with a prefactor $A = 0.47$ which is consistent with the experimental and numerical results of Deblais et al. [32]. For the ~ 260 times more viscous solvent in figure 3(f), the self-similar regime is well captured by the visco-capillary thinning law [33, 34]

$$h = 0.0709 \frac{\gamma}{\eta_0} (t_c - t). \quad (21)$$

This is consistent with the fact that the Ohnesorge number $Oh = \eta_0 / \sqrt{\rho \gamma h_0}$ (see equation 5) is up to 0.02 for PEO_{aq} and up to 0.1 for HPAM (for the smallest plate diameter where h_0 is lowest), i.e. $Oh \ll 1$, and ranges between 1.0 and 1.9 for the $\text{PEO}_{\text{visc},1}$ solution in the range of plate diameters considered in figure 3. In spite of the moderate Ohnesorge numbers in the latter case, we do not observe a clear transition to the inertio-visco-capillary thinning law $h = 0.0304(\gamma/\eta_0)(t_c - t)$ [35, 36] which describes the behaviour of Newtonian fluids close to breakup, see figure 3(d).

Interestingly, the transition to the elastic regime occurs around the time at which the self-similar Newtonian regime is reached in figure 3(d,f), slightly after for the $\text{PEO}_{\text{aq},1}$ solution and slightly before for the $\text{PEO}_{\text{visc},1}$ solution. However, in both cases, the transition radius $h_1 = h(t_1)$ increases with the plate diameter $2R_0$, which indicates that polymers already started to significantly deform before the self-similar regime. Indeed, if polymers only started to deform within the self-similar regime where the thinning dynamics does not depend on R_0 or V^* anymore, the amount of polymer deformation would be independent on the initial condition, leading to a transition radius h_1 which would not depend on R_0 or V^* , as we discuss further in §4.3.

After the filament formation, the thinning rate $|\dot{h}/h|$ is initially fairly constant, indicating an exponential decay, and increases close to breakup in a so-called ‘terminal regime’ where authors argue that polymer chains approach full extension and a Newtonian-like high-viscosity dynamics is recovered [9, 19, 37, 38]. The (constant) filament thinning rate measured during the exponential part of the elastic regime is found to decrease with increasing plate diameter, see figure 3(c,e). This is inconsistent with the Oldroyd-B model which predicts $|\dot{h}/h| = 1/3\tau$ (see equation 1) where τ is the (longest) relaxation time of the polymer solution which is a fluid property, independent of the size of the system. As we show in our previous paper [21],

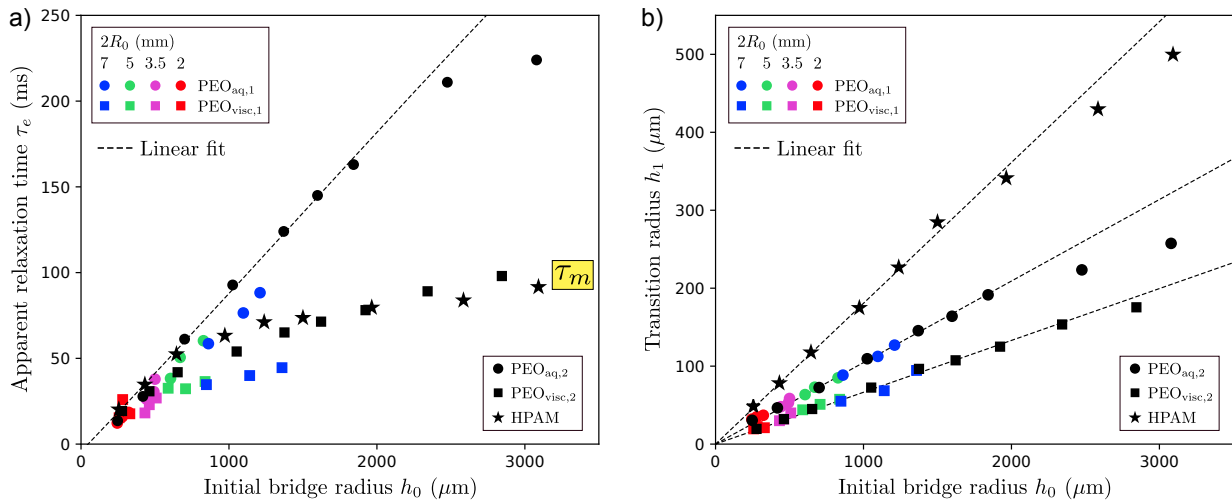


Figure 4: Effective extensional relaxation time τ_e (a) and transition radius h_1 (b) against the last stable bridge radius h_0 for different plate radii R_0 and droplet volumes V^* for all polymer solutions. For the $\text{PEO}_{\text{aq},1}$ and the $\text{PEO}_{\text{visc},1}$ solutions, three points of the same colour correspond to the same R_0 and three different V^* .

this surprising dependence on the system size is also observed for the classical step-strain plate separation protocol of a commercial CaBER rheometer as well as for Dripping-onto-Substrate and dripping [13] experiments. We show that this is not caused by artefacts such as solvent evaporation or polymer degradation, suggesting that the liquid does not change when being tested with different plate diameters. To discuss this geometry-dependent filament thinning rate, we define an apparent (or effective) relaxation time τ_e such that $|\dot{h}/h| = 1/3\tau_e$ during the exponential part of the elastic regime.

The apparent relaxation time τ_e and the transition radius h_1 are plotted against h_0 in figure 4 for different polymer solutions, plate diameters $2R_0$ and droplet volumes V^* . The fact that data corresponding to different values of R_0 and V^* collapse on a single curve for both the $\text{PEO}_{\text{aq},1}$ and the $\text{PEO}_{\text{visc},1}$ solutions suggests that h_0 , which is an increasing function of both R_0 and V^* (see figure 2(b)) is the only relevant geometrical parameter of the problem. This is the reason why we chose h_0 at the relevant length scale for non-dimensional numbers such as the Ohnesorge and Deborah numbers in equations 5 and 6. This is in agreement with the idea that the thinning dynamics is only influenced by extensional flow in the bridge / filament while the top and bottom end droplets act as passive liquid reservoirs.

We find that τ_e seems to saturate towards a maximum value τ_m at large h_0 , see figure 4(a). The estimated values of τ_m are reported in table 2 for the $\text{PEO}_{\text{aq},2}$, $\text{PEO}_{\text{visc},2}$ and HPAM solutions for which plate diameters up to 25 mm were used, well beyond typical CaBER plate sizes, which was needed to observe the saturation of τ_e . In our previous paper [21], we explored the possibility that τ_m could be the ‘real’ relaxation time of the solution,

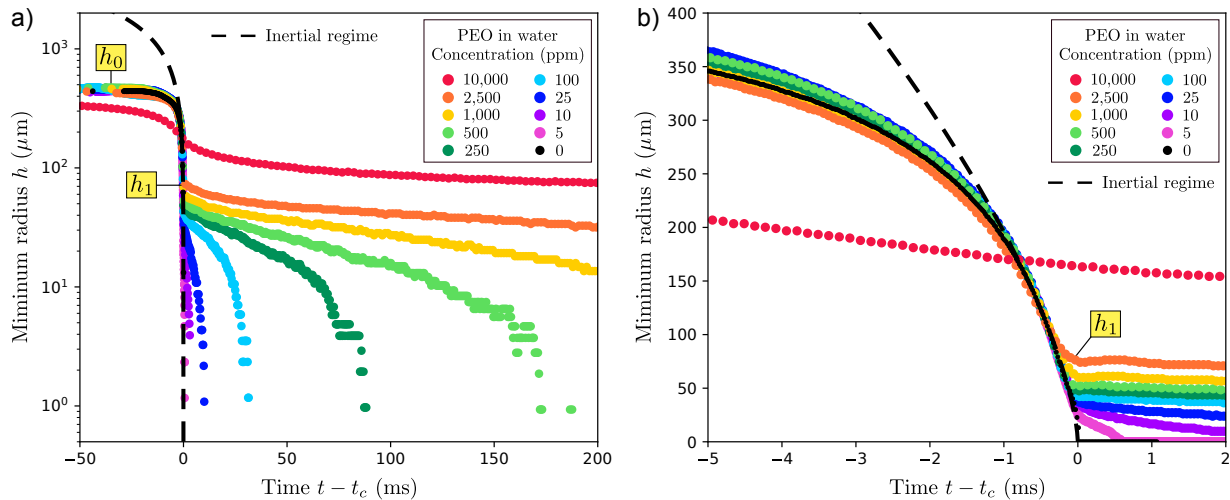


Figure 5: Time evolution of the minimum bridge/filament radius h in lin-log (a) and lin-lin, focusing on the first transition (b), for PEO-4M solutions of different concentrations in water, for a fixed plate diameter $2R_0 = 3.5$ mm and drop volume $V^* \approx 2.4$. The time t_c is the time at which the bridge would break up for the solvent alone, here water.

invoking finite extensibility effects described by the FENE-P model to explain thinning rates larger than $1/3\tau_m$ for low h_0 . We concluded that this was a possible explanation only for the $\text{PEO}_{\text{visc},2}$ solution but not for the $\text{PEO}_{\text{aq},2}$ and HPAM solutions, suggesting that the FENE-P model misses some important features of polymer dynamics in extensional flows.

The first transition radius h_1 increases fairly linearly with h_0 for all liquids, see figure 4(b). This is in contradiction with the scaling $h_1 \propto h_0^{4/3}$ expected from the Oldroyd-B model when assuming that polymer relaxation is negligible during the time needed for the bridge to thin from h_0 to h_1 , see equation 2. Since $h_0 \propto R_0$ for a fixed V^* (see figure 2(b)), this implies that $h_1 \propto R_0$, different from the scaling $h_1 \propto R_n^{0.66}$ observed experimentally by Rajesh et al. [13] in the analogous problem of a drop falling from a nozzle of radius R_n . This is surprising since R_n should play the same role as the plate radius R_0 in CaBER.

Note that the $\text{PEO}_{\text{aq},2}$ and $\text{PEO}_{\text{visc},2}$ solutions are slightly more elastic than the $\text{PEO}_{\text{aq},1}$ and $\text{PEO}_{\text{visc},1}$ solutions since they exhibit larger apparent relaxation times, see figure 4(a). However, these differences are barely visible in 4(b) since the values of h_1 are almost the same, suggesting that the dependence of h_1 on τ_e is relatively weak, as we now confirm by varying the polymer concentration.

3.2. Influence of the polymer concentration

Figure 5 shows the time evolution of the minimum bridge / filament radius for the aqueous PEO solutions of table 1 of various PEO concentrations, water solvent included, which were

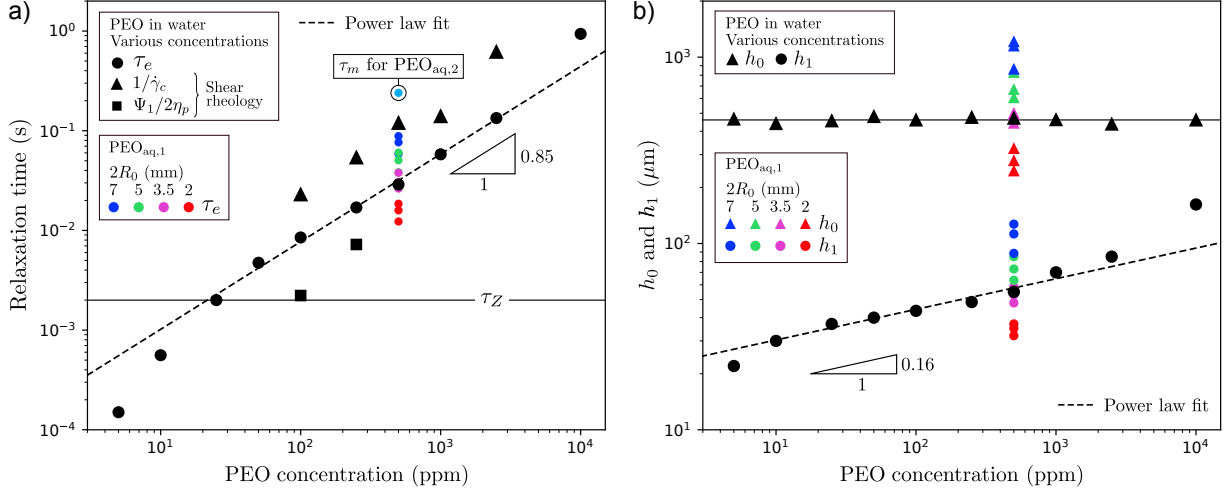


Figure 6: (a) Relaxation times and (b) transition radius h_1 and last stable bridge radius h_0 against polymer concentration for PEO-4M solutions of different concentrations in water. The data of panel (b) and the effective CaBER relaxation time τ_e in panel (a) correspond to a fixed plate diameter $2R_0 = 3.5$ mm and drop volume $V^* \approx 2.4$, except for the 500 ppm solution where data corresponding to different $2R_0$ (between 2 and 7 mm) and V^* are shown. In panel (a), we also plot the relaxation time $1/\dot{\gamma}_c$ and $\Psi_1/2\eta_p$ from shear rheology, as well as the Zimm relaxation time τ_Z . We also show the maximum CaBER relaxation time τ_m (high h_0 limit of τ_e) measured for the (500 ppm) PEO_{aq,2} solution (which is slightly more elastic than the PEO_{aq,1} solution from which the other 500 ppm data points are from, see figure 4(a)).

tested for a fixed plate diameter $2R_0 = 3.5$ mm and droplet volume $V^* \approx 2.4$, in semi-log (figure 5(a)) and in lin-lin focusing on the transition to the elastic regime (figure 5(b)). Like figure 3, the time t_c at which the solvent breaks is chosen as the time reference and curves corresponding to polymer solutions are shifted along the time axis to maximise the overlap with the solvent for $t < t_1$. This overlap is very good up to 2,500 ppm (dilute and unentangled semi-dilute solution), small deviations being attributable to slightly different droplet volumes. For 10,000 ppm however (entangled semi-dilute solutions), the bridge dynamics prior to the exponential regime is radically different from the pure solvent case, indicating that elasticity is not negligible even before the exponential regime is reached.

The apparent relaxation time τ_e and the transition radius h_1 are plotted in figure 6 as a function of the polymer concentration c for the aqueous PEO solutions of table 1. Since these solutions were tested for a fixed plate diameter $2R_0 = 3.5$ mm and droplet volume $V^* \approx 2.4$, the initial bridge radius $h_0 \approx 460$ μm , also plotted in figure 6(b), is the same for each solution. For the 500 ppm solution, labelled PEO_{aq,1}, which was tested for four plate diameters from 2 to 7 mm and, in each case, with three different volumes, the corresponding values of τ_e , h_0 and h_1 are also included in figure 6 to illustrate how data for a given concentration can shift as h_0 is varied. Although not large enough plate diameters were used to estimate the

high- h_0 limit value τ_m of the relaxation time for the PEO_{aq,1} solution, the value estimated for the slightly more elastic PEO_{aq,2} solution (see figure 4(a) and table 2) is shown in 6(a) for 500 ppm.

We find a weak dependence $h_1 \propto c^{0.16}$ for dilute and semi-dilute solutions, see figure 6(b), consistent with Rajesh et al. [13] who found $h_1 \propto c^{0.15}$ in the analogous problem of a drop falling from a nozzle. We find a power law $\tau_e \propto c^{0.85}$ for the apparent relaxation time in figure 6(a), consistent with the wide range of exponents, typically between 0.6 and 1, reported by other authors in CaBER [8, 39, 40] and pendant drop experiments [12, 13]. Note that this exponent is expected to be a function of the solvent quality [40] and that its potential dependence on h_0 is not investigated in the present work. From these scalings, we deduce a weak dependence of $h_1 \propto \tau_e^{0.19}$ on the apparent relaxation time.

The apparent CaBER relaxation time τ_e in figure 6(a) is compared to values estimated from shear rheology, i.e. $1/\dot{\gamma}_c$ which is estimated from shear viscosity curves featuring shear-thinning, which excludes low concentrations, and $\Psi_1/2\eta_p$ which is estimated from the first normal stress difference for the only two measurable solutions exhibiting a quadratic scaling $N_1 \propto \dot{\gamma}^2$. We observe that $1/\dot{\gamma}_c$ follows a power law with an exponent close to the one found for τ_e . Additionally, we find that τ_e is larger than $\Psi_1/2\eta_p$ in figure 6(a) for this specific plate radius, and would hence be even larger in the high- h_0 limit τ_m . Hence, even for dilute solutions exhibiting weak shear-thinning and quadratic normal stresses, for which the Oldroyd-B model could describe the shear rheology, there is no quantitative agreement between the relaxation time measured from normal stresses and from filament thinning rheometry, in agreement with Zell et al. [39] who dedicated a paper specifically on the link between τ_e and Ψ_1 . The discrepancy between relaxation times measured in shear and in extension likely (partially) stems from the fact that elastic dumbbell models such as Oldroyd-B and FENE-P predict that polymer chains approach full extension in strong shear flows ($\tau\dot{\gamma} \gg 1$), in contradiction with the tumbling-motion-induced partial extension observed experimentally [41]. In a perspective paper currently under preparation, Boyko & Stone suggest that comparing shear and extension-derived model parameters should therefore be done using more complex models such as the FENE-PTML model (so named by the authors) proposed by Phan-Thien, Manero, and Leal [42] which captures this partial extension under shear. In this paper, we only consider filament thinning extensional flows for which Oldroyd-B and FENE-P are suitable model candidates.

As shown in figure 6(a), the apparent CaBER relaxation time τ_e increases in the dilute regime $c < c^*$ and, for the most dilute solutions, is less than the Zimm relaxation time calculated using

$$\tau_Z = \frac{1}{\zeta(3\nu)} \frac{[\eta]M_w\eta_s}{N_a k_B T}, \quad (22)$$

where N_a is the Avogadro number, k_B the Boltzmann constant, T the temperature, ζ the

Riemann zeta function and ν the solvent quality exponent. We used $\nu = 0.55$ between theta and good solvent to find $\tau_Z = 2.0$ ms. Similar results were reported by Clasen et al. [40] who argue that the increase of τ_e in the dilute regime is caused by a self-concentration effect where chains start to interact while unravelling well beyond their equilibrium size in strong extensional flows, as was later rationalised by Prabhakar et al. [43]. Clasen et al. and Prabhakar et al., who only considered cases where inertia was negligible in the Newtonian regime, also show that values of $\tau_e < \tau_Z$ arise at low polymer concentration where elasticity is too weak to fully overcome the solvent viscosity in the elastic regime. This effect should however be negligible for the aqueous PEO solutions of figure 6(a) since it is inertia (and not the solvent viscosity) that dominates in the Newtonian regime (see figure 5(b)). We show in §5 that values of $\tau_e < \tau_Z$ at low concentrations are consistent with polymer chains approaching their finite extensibility limit at the onset of the elastic regime (as anticipated by Campo-Deaño & Clasen [19]), a case where equation 1 is no longer valid and filament thinning rates $|\dot{h}/h| > 1/3\tau$ are to be expected as we show in our previous paper [21].

4. Oldroyd-B prediction for h_1

In this section, we expand the polymer-relaxation-free theory leading to equation 2 for h_1 to cases where polymer relaxation is not negligible in the Newtonian regime. The generalised Oldroyd-B prediction for h_1 is derived theoretically in §4.1, tested against experimental results in §4.2 and validated numerically in §4.3.

4.1. Theory

The filament radius $h_1 = h(t_1)$ marks the transition between the Newtonian regime ($t < t_1$), where the driving capillary force is balanced by inertia and/or viscosity, and the elastic regime ($t > t_1$) where capillarity is balanced by elastic stresses arising from the stretching of polymer chains. If inertia is negligible, slender filament theory predicts that the total (unknown) tensile force T is constant along the liquid column (bridge or filament) [16, 36] which, neglecting gravity and axial curvature effects, results in the zero-dimensional force balance equation [40]

$$(2X - 1)\frac{\gamma}{h} = 3\eta_s\dot{\epsilon} + \sigma_{p,zz} - \sigma_{p,rr} \quad (23)$$

for a column of radius h . The driving capillary pressure γ/h is balanced by the normal stress difference $\sigma_{zz} - \sigma_{rr}$ which is the sum of the solvent viscous stress $3\eta_s\dot{\epsilon}$ and of the polymeric stress $\sigma_{p,zz} - \sigma_{p,rr}$ where $\dot{\epsilon} = -2\dot{h}/h$ is the extension rate, the dot standing for d/dt, and where z is the direction of the flow. The ratio $X = T/2\pi\gamma h$ may vary over time, approaching $X = 0.7127$ for a Newtonian fluid [34], hence recovering equation 21 close to breakup, and

approaching $X = 3/2$ in the elastic regime for an Oldroyd-B fluid [44] (and not 1 as originally proposed in [15]). When inertia is not negligible, Tirtaatmadja et al. suggested adding a term of the form $\frac{1}{2}\rho\dot{h}^2$ to equation 23 [12], from which the inertio-capillary scaling of equation 20 is recovered. In the elastic regime ($t > t_1$), assuming that inertia and/or solvent viscosity has become negligible, and assuming that the axial stress dominates over the radial stress, i.e. $|\sigma_{p,rr}| \ll |\sigma_{p,zz}|$, the force balance equation reduces to

$$(2X - 1)\frac{\gamma}{h} = \sigma_{p,zz}. \quad (24)$$

The elastic regime starts when the polymeric axial stress $\sigma_{p,zz}$, which increases over time in the Newtonian regime as polymer chains are progressively stretched by the extensional flow in the thinning bridge, becomes of the order of the capillary pressure, say, when it is equal to fraction p of the capillary pressure (Campo-Deaño & Clasen chose $p = 1/2$ [19]). We hence get that $p\gamma/h_1 = \sigma_{p,zz}(t = t_1)$ where, for simplicity, the prefactor $2X - 1$ of order unity has been included in the prefactor p . To estimate h_1 , we hence need to choose a constitutive equation to express the polymeric stress. Since our main goal is to understand the effect of polymer relaxation during the Newtonian regime on h_1 which, when negligible, leads to equation 2 for a single-mode Oldroyd-B fluid, we choose to use this model for simplicity. Indeed, although we know that the Oldroyd-B model is unable to capture the system-size dependence of the apparent relaxation time τ_e discussed in our previous paper [21] (see also figure 3 and 4(a)), it is not yet clear whether it is able capture h_1 or not. Finite extensibility effects on h_1 will be discussed in §5 using the FENE-P model.

For an Oldroyd-B fluid with elastic modulus G , we have $\sigma_{p,zz} = G(A_{zz} - 1)$ where A_{zz} is the normal part of the conformation tensor \mathbf{A} which follows (see equation 14 and [45])

$$\dot{A}_{zz} - 2\dot{h}A_{zz} = -\frac{A_{zz} - 1}{\tau}, \quad (25)$$

where τ is the relaxation time. Since we are interested in the location of highest polymer extensions along the bridge, we use the expression of the extension rate $\dot{h} = -2\dot{h}/h$ at the thinnest point to obtain

$$\dot{A}_{zz} + \frac{4\dot{h}}{h}A_{zz} = -\frac{A_{zz} - 1}{\tau}. \quad (26)$$

Some (yet unknown) time after the onset of capillary thinning of the liquid bridge, polymer chains will have stretched well beyond their equilibrium size, i.e. $A_{zz} \gg 1$, at which point equation 26 can be integrated into

$$A_{zz}h^4 \propto e^{-t/\tau}, \quad (27)$$

with a (yet unknown) constant prefactor. Combining equations 27 and 24 leads to the exponential decay $h \propto e^{-t/3\tau}$ described by equation 1. Polymer chains are expected to remain

close to their equilibrium coiled size (A_{zz} close to 1) until the extension rate in the thinning bridge approaches the coil-stretch transition value $1/2\tau$ predicted by the Oldroyd-B model. Beyond this point, following Clasen et al. [19, 46], we assume that polymer chains unravel with negligible relaxation, i.e., that the right-hand side of equation 26 becomes negligible so that $A_{zz}h^4$ becomes constant. More precisely,

$$A_{zz}h^4 = H^4, \quad (28)$$

where H is the (yet unknown) bridge radius at which relaxation becomes negligible, which should correspond to the coil-stretch transition point at which A_{zz} starts to become significantly larger than 1. In particular, at the transition to the elastic regime at time $t = t_1$,

$$A_1 = (H/h_1)^4, \quad (29)$$

where $A_1 = A_{zz}(t_1)$ quantifies the amount of polymer stretching at the onset of the elastic regime. Since $p\gamma/h_1 = \sigma_{p,zz}(t_1) = GA_1$, we finally get that

$$h_1 = \left(\frac{GH^4}{p\gamma} \right)^{1/3}, \quad (30)$$

which is different from equation 2. Indeed, H is only equal to h_0 in the limit where polymer relaxation is negligible throughout the whole Newtonian regime so that $A_{zz}h^4$ is constant and equal to h_0^4 since $A_{zz} = 1$ at the onset of capillary thinning, assuming no pre-stress. In other words, $H = h_0$ means that the coil-stretch transition starts at the onset of capillary thinning. This is only true if the relaxation time τ is much larger than the time taken by the liquid bridge to thin from h_0 to h_1 , as we detail below.

4.2. Experiments

In order to test the validity of the Oldroyd-B prediction (equation 30) for h_1 , we first need to compute H from the time-evolution of A_{zz} . Note that we do not experimentally measure the extension of polymer chains, unlike Ingremeau & Kellay [47] who confirmed the transition from a coiled to a stretched state in viscoelastic pinch-off using fluorescently labelled DNA. Rather, since our goal is to test a specific constitutive equation, here Oldroyd-B, we calculate its prediction for $A_{zz}(t)$ using equation 26 where the extension rate $\dot{\epsilon} = -2\dot{h}/h$ is taken from experimental values of $h(t)$. In other words, we calculate the prediction of the model for the experimental history of extension rates in the bridge / filament. In particular, we do *not* assume large polymer extension ($A_{zz} \gg 1$) since the point at which A_{zz} starts to become significantly larger than 1 is precisely what sets H . Equation 26 can in fact be integrated, as

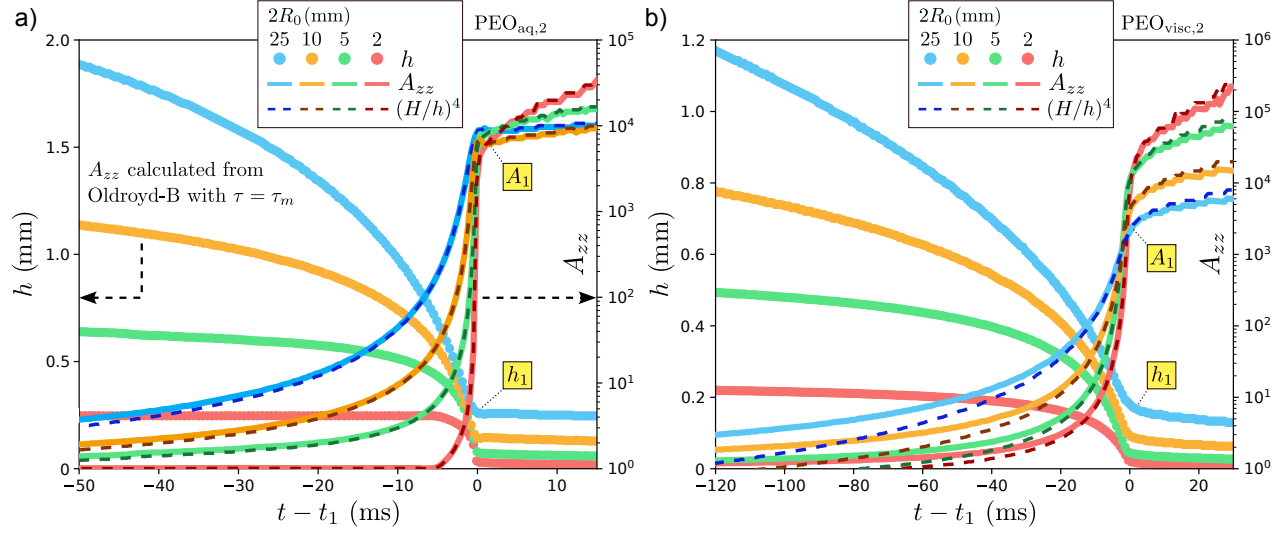


Figure 7: Time evolution of the experimental minimum filament / bridge radius h and of A_{zz} , calculated from the Oldroyd-B prediction (equation 31) using the experimental values of $h(t)$ with the choice of relaxation time $\tau = \tau_m$ (see figure 4(a)), for plate diameters $2R_0 = 2, 5, 10$ and 25 mm for the PEO_{aq,2} (a) and the PEO_{visc,2} (b) solutions. Time t_1 marks the onset of the elastic regime, with $h_1 = h(t_1)$ and $A_1 = A_{zz}(t_1)$. Values of A_{zz} in the Newtonian regime ($t < t_1$) are compared to $(H/h)^4$ (see equation 28) where H is used as a fitting parameter to optimise the agreement close to t_1 .

shown by Bazilevsky et al. [48], introducing a function $y(t)$ such that $A_{zz} = y \exp(-t/\tau)/h^4$, which leads to $\dot{y} = h^4 \exp(t/\tau)/\tau$, yielding

$$A_{zz} = \frac{e^{-t/\tau}}{h^4} \left(h_0^4 e^{t_0/\tau} + \frac{1}{\tau} \int_{t_0}^t h^4(t') e^{t'/\tau} dt' \right), \quad (31)$$

where the initial time t_0 corresponds to the onset of capillary thinning, i.e. $h(t_0) = h_0$ and $A_{zz}(t_0) = 1$ (no pre-stress). Since the $h(t)$ history is set by the experimental data, the only adjustable parameter of equation 31 is the relaxation time τ . In the following, we either use the apparent (τ_e) or the maximum (τ_m) relaxation time measured experimentally (see figure 4(a)) to calculate A_{zz} since we still do not know which one is the ‘true’ one, if any.

Values of $A_{zz}(t)$ computed from equation 31 using the experimental values of $h(t)$ with relaxation time $\tau = \tau_m$ are shown in figure 7(a) for the PEO_{aq,2} solution and in figure 7(b) for the PEO_{visc,2} solution for plate diameters $2R_0$ between 2 and 20 mm. The experimental values of $h(t)$ are shown on the left y-axis and the time reference t_1 corresponds to the onset of the elastic regime. We find that the amount of polymer extension $A_1 = A_{zz}(t_1)$ at the onset of the elastic regime is fairly independent of the initial condition for the PEO_{aq,2} while, for the PEO_{visc,2} solution, A_1 decreases as $h_0(R_0, V^*)$ increases, as mentioned in our previous

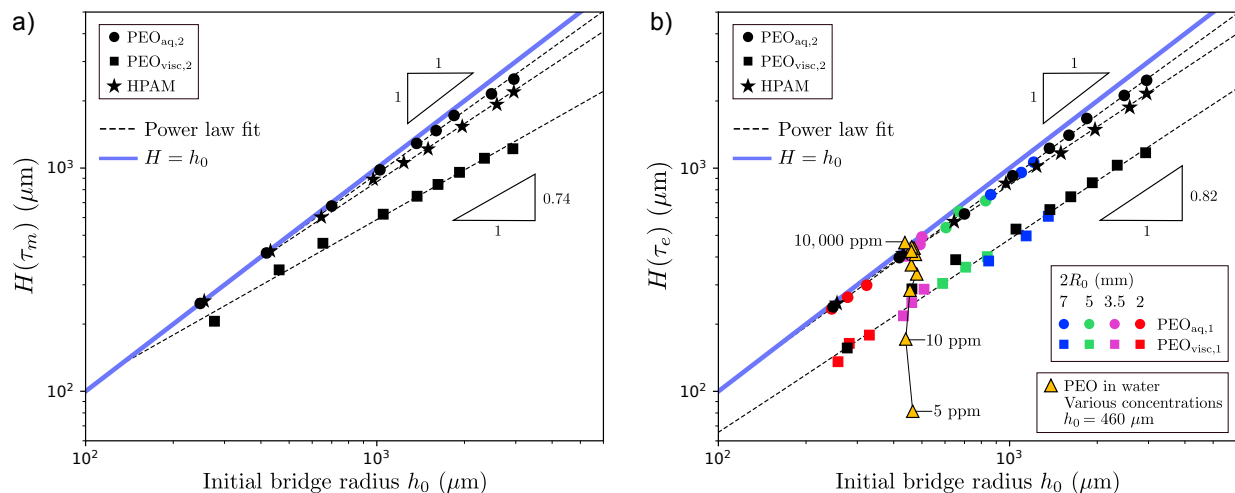


Figure 8: Values of H calculated from the time evolution of A_{zz} from Oldroyd-B (see figure 7) using the maximum relaxation time $\tau = \tau_m$ (a) or the effective relaxation time $\tau = \tau_e$ (b) for different polymer solutions and initial bridge radii $h_0(R_0, V^*)$, plotted against h_0 . The line $H = h_0$ is shown in both panels.

paper [21] and as we are about to discuss here in more depth. In any case, we find that A_{zz} always increases as $1/h^4$ in the Newtonian regime close enough to the transition to the elastic regime. More specifically, values of A_{zz} are well captured by $(H/h)^4$ using H as a fitting parameter for each data set (close to t_1), from which H is estimated, see figure 7.

Values of H calculated using $\tau = \tau_m$, named $H(\tau_m)$, are plotted against h_0 in figure 8(a) for the $\text{PEO}_{\text{aq},2}$, $\text{PEO}_{\text{visc},2}$ and HPAM solutions which are the only solutions for which sufficiently large plate diameters were used to estimate the maximum relaxation time τ_m (the high- h_0 limit of τ_e , see figure 4(a)). For the $\text{PEO}_{\text{aq},2}$ and HPAM solutions, we find that H is essentially equal to h_0 at low h_0 and that H/h_0 decreases as h_0 increases, down to 0.73 for the largest plate diameter. In contrast, for the $\text{PEO}_{\text{visc},2}$ solution, the ratio H/h_0 takes significantly smaller values, decreasing from 0.56 to 0.40 as h_0 increases. This is why the $(H/h)^4$ fit for A_{zz} is fairly good throughout the whole Newtonian regime for the $\text{PEO}_{\text{aq},2}$ solution in figure 7(a) while it is only valid within a small time window close to the transition to the elastic regime for the $\text{PEO}_{\text{visc},2}$ solution in figure 7(b). Indeed, if $H = h_0$, then the $(H/h)^4$ fit for A_{zz} is even valid at the onset of capillary thinning where $h = h_0$ and $A_{zz} = 1$.

Figure 8(a) hence suggests that, although all three solutions have comparable relaxation times (see figure 4(a)), the thinning dynamics in the Newtonian regime is such that polymer chains stretch almost without relaxing in the Newtonian regime for the low solvent viscosity solutions ($\text{PEO}_{\text{aq},2}$ and HPAM) while relaxation is not negligible for the high solvent viscosity ($\text{PEO}_{\text{visc},2}$) solution. This is because the Newtonian thinning dynamics is slower for the most viscous solution, see, e.g., figure 7 where, for $2R_0 = 2$ mm, the bridge takes only about

6 ms to thin from h_0 to h_1 for the PEO_{aq,2} solution, much less than τ_m (chains do not have enough time to relax), while it takes about 900 ms for the PEO_{visc,2}, much more than τ_m (not visible in figure 7(b) where we focus on times close to t_1). The fact that H/h_0 increases as h_0 increases can therefore be interpreted by a longer time to thin from h_0 to h_1 as h_0 increases, consistent with the fact that the Rayleigh and viscous time scales $\tau_R = \sqrt{\rho h_0^3/\gamma}$ and $\tau_{\text{visc}} = \eta_0 h_0/\gamma$ both increase with h_0 .

The dependence of H on h_0 and on the solvent viscosity explains why, in figure 7 and in our previous paper [21], A_1 is independent of h_0 for low solvent viscosity solutions (PEO_{aq,2} and HPAM) while A_1 decreases as h_0 increases for the high solvent viscosity solution (PEO_{visc,2}). For the former where H is close to h_0 (negligible polymer relaxation in the Newtonian regime), $A_1 = (H/h_1)^4$ (see equation 29) is close to $(h_0/h_1)^4$ which is fairly constant since $h_1 \propto h_0$ according to figure 4(b). For the latter however, where $H \propto h_0^{0.74}$ in our range of h_0 according to figure 8(a), we get $A_1 = (H/h_1)^4 \propto h_0^{-1.04}$.

In figure 8(b) we plot the values of H , named $H(\tau_e)$, calculated using the apparent relaxation time $\tau = \tau_e$ when computing A_{zz} from equation 31 (instead of its large- h_0 limit τ_m in figure 8(a)). All polymer solutions are now featured since τ_e is measured for any experiment from an exponential fit of $h(t)$ in the exponential part of the elastic regime (see figure 3), i.e., the PEO_{aq,2}, PEO_{visc,2} and HPAM solutions, like in figure 8(a), but also the PEO_{aq,1} and PEO_{visc,1} solutions, where three different non-dimensional droplet volumes V^* were tested for each of the four smallest plate diameters, as well as the PEO solutions in water with various polymer concentration (table 1) which were tested for a single (R_0, V^*) set corresponding to $h_0 \approx 460 \mu\text{m}$. The data corresponding to the PEO solutions with different polymer concentrations c show how, for a given flow history in the Newtonian regime (same $h(t)$ curves for $t < t_1$ for all concentrations, see figure 5), H increases with c via the increase in the relaxation time (here $\tau = \tau_e$), reaching the upper limit value h_0 at large τ . This is because, for large τ values, polymer relaxation is negligible throughout the whole Newtonian regime while, for low τ values, A_{zz} remains equal to 1 for most of the Newtonian regime, only increasing when $\dot{\epsilon}$ finally gets of the order of $1/2\tau$ close to the transition to the elastic regime.

Now that we know the value of H , we can test the validity of equation 30 for the filament radius h_1 at the onset of the elastic regime. The value of the elastic modulus, $G = \eta_p/\tau$ in the Oldroyd-B model, is however not uniquely defined since, while $\eta_p = \eta_0 - \eta_s$ can be calculated unambiguously from the shear rheology, the relaxation time τ could either be the apparent one τ_e or the maximum one τ_m since we do not know yet which one is the ‘true’ one, if any. We hence need to test for both. To this end, we define

$$G_H = \gamma h_1^3/H^4, \quad (32)$$

where h_1 is the value measured experimentally, which should be $G_H = G/p$ according to

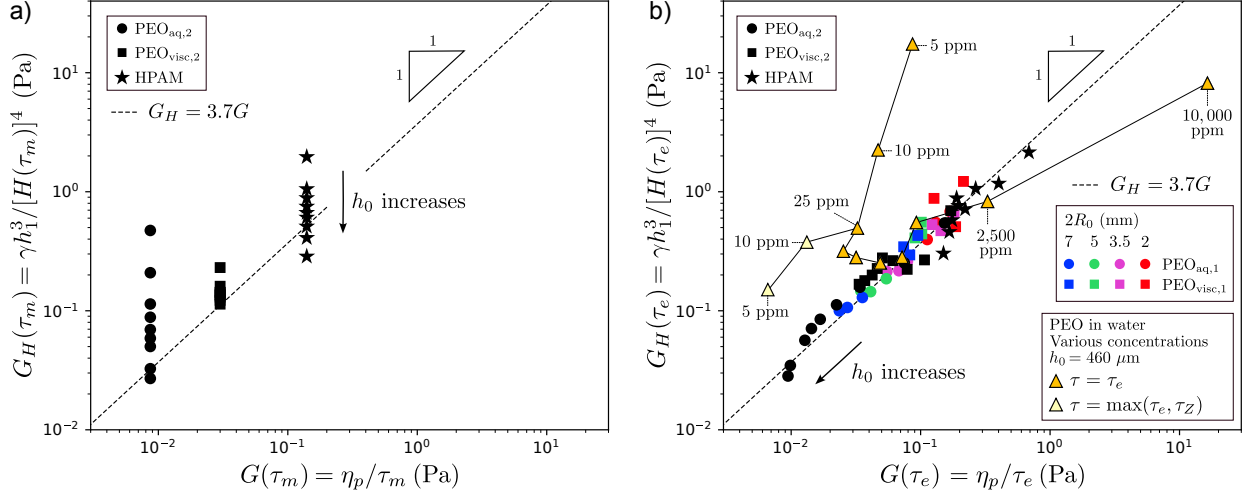


Figure 9: G_H defined in equation 32 against the elastic modulus $G = \eta_p/\tau$ where H and G are calculated from the maximum relaxation time $\tau = \tau_m$ (a) or the effective relaxation time $\tau = \tau_e$ (b) for various polymer solutions and initial bridge radii $h_0(R_0, V^*)$. Values of h_1 are the one measured experimentally. In panel (b), for the aqueous PEO solutions of different concentrations (see table 1), we show the effect replacing τ_e by the Zimm relaxation time τ_Z when calculating G and H for the lowest concentrations $c = 5$ and 10 ppm which exhibit values of $\tau_e < \tau_Z$, see figure 6(a). The line $G_H = 3.7G$ is shown in both panels.

equation 30.

In figure 9(a), G_H is plotted against G for the choice of relaxation time $\tau = \tau_m$ for the $\text{PEO}_{\text{aq},2}$, $\text{PEO}_{\text{visc},2}$ and HPAM solutions which are the only solutions for which sufficiently large plate diameters were used to estimate τ_m . More precisely, values of $G_H(\tau_m)$ calculated from $H(\tau_m)$ are plotted against $G(\tau_m) = \eta_p/\tau_m$ which takes a unique value for each solution since the relaxation time is unique. We find that values of $G_H(\tau_m)$ are, however, not unique for the $\text{PEO}_{\text{aq},2}$ and HPAM solutions and monotonously decrease as h_0 is increases. For the $\text{PEO}_{\text{visc},2}$ however, values of G_H vary between 0.11 and 0.23 without clear monotonic trend as h_0 increases. This is because, since $h_1 \propto h_0$ and $H \propto h_0^{k_H}$ in the range of h_0 values investigated with $k_H \leq 1$ (see figures 4(b) and 8(a)), $G_H \propto h_1^3/H^4 \propto h_0^{3-4k_H}$ which means that G_H is only expected to be independent of h_0 for $k_H = 0.75$, very close to the value 0.74 found for the $\text{PEO}_{\text{visc},2}$ solution in figure 8(a). This suggests that the prediction of equation 30 for the choice $\tau = \tau_m$ is only potentially valid for one of our three solutions, the most dilute and viscous one.

By contrast, as shown in figure 9(b), when choosing τ_e instead of τ_m for the relaxation time to calculate $G_H(\tau_e)$ from $H(\tau_e)$ and $G(\tau_e) = \eta_p/\tau_e$, data points fall on a single curve for all three solutions ($\text{PEO}_{\text{aq},2}$, $\text{PEO}_{\text{visc},2}$ and HPAM) as well as for the $\text{PEO}_{\text{aq},1}$ and $\text{PEO}_{\text{visc},1}$ solutions (for which V^* is varied for the four smallest plate diameters) and we find the linear

relationship $G_H = G/p$ predicted by equation 30 with $p \approx 0.27$. It is quite remarkable that the Oldroyd-B model, derived for ideal dilute chains, is able to capture the transition to the elastic regime for solutions that are as diverse in terms of solvent viscosity, concentration and, potentially, solvent quality exponents.

Strong deviations from the $G_H = 3.7G$ line can be observed in figure 9(b) at low polymer concentrations for the data corresponding to the PEO solutions with various polymer concentrations. This data set can be broken down into three subsets: for typically $c < 100$ ppm, G_H decreases sharply with concentration while is it almost constant for $100 \text{ ppm} \leq c < 2,500$ ppm and increases sharply with concentration for $c \geq 2,500$ ppm. These trends can be explained by the fact that $G_H \propto h_1^3/H^4$ where h_1 increases very slowly with concentration as $h_1 \propto c^{0.16}$ for $c < 2,500$ ppm and increases sharply for higher concentrations (see figure 6(b)) while H increases sharply with concentration for typically $c < 100$ ppm, becoming almost constant and equal to h_0 for larger concentrations (see figure 8(b)). These strong deviations from the $G_H = 3.7G$ line observed at low polymer concentrations in figure 9(b) could be partially explained by the fact that apparent relaxation times (measured from exponential fitting of $h(t)$) are less than the Zimm relaxation time $\tau_Z = 2$ ms for $c = 5$ and 10 ppm (see figure 6(a)). In figure 9(b), we show the effect of choosing $\tau = \tau_Z$ instead of τ_e as the relaxation time for $c = 5$ and 10 ppm, which changes the value of both G_H via $H(\tau)$ and of $G = \eta_p/\tau$. We find that this correction leads to data points significantly closer to the $G_H = 3.7G$ line, mainly stemming from larger values of H than in figure 8(b), although one order of magnitude deviation from the $G_H = 3.7G$ line still remains. We show in §5 that finite extensibility effects can explain this deviation (i.e. values of h_1 higher than the Oldroyd-B prediction) as well as the values of $\tau_e < \tau_Z$ for low polymer concentrations.

The large deviation from the $G_H = 3.7G$ line for the entangled 10,000 ppm solution in figure 9(b) (the only solution for which polymers affect the thinning dynamics even before the exponential regime, see figure 5), is probably due to the fact that such solutions cannot be described by non-interacting polymer theories such as Oldroyd-B.

In conclusion, when polymer relaxation is not negligible in the Newtonian regime ($t < t_1$), equation 2 should be replaced by equation 30 which gives $h_1 \propto H^{4/3}$ where $H \leq h_0$. In our experiments, the power law dependence of H on h_0 (see figure 8) leads to the fairly proportional relationship between h_1 and h_0 observed in figure 4(b), differences in slopes among different liquids stemming from differences in elastic moduli G . In §4.3, we discuss how H scales with the parameters of the problem using numerical simulations.

4.3. Simulations

To further investigate the effect of polymer relaxation on the transition radius h_1 marking the onset of the elastic regime, we now consider numerical simulations using the Oldroyd-B model ($L^2 = +\infty$) with a single relaxation time τ (finite extensibility effects will be discussed

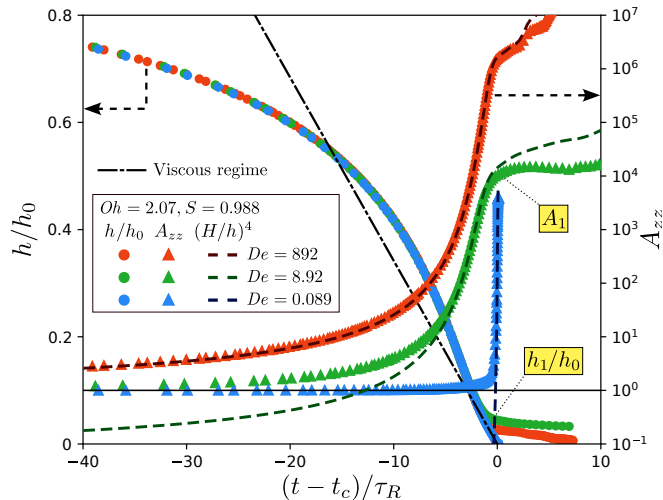


Figure 10: Numerical time evolution of the non-dimensional (minimum) bridge / filament radius h/h_0 and of the (maximum) polymer extension A_{zz} for $Oh = 2.07$, $S = 0.988$ and $h_0/R_0 = 0.23$ and three different Deborah numbers. A_{zz} is compared with $(H/h)^4$ where H is used as a fitting parameter. The self-similar viscous regime of equation 21, or equivalently $h/h_0 = 0.0709(t_c - t)/(Oh\tau_R)$, is also plotted, where t_c is the time at which the filament would break if the transition to an elastic regime, at $h = h_1$, did not occur.

in §5). In this paper, numerical simulations are not directly compared to experiments but are rather used to validate theoretical expressions which are then compared with experiments (see our previous paper for direct experiment-simulation comparisons [21]).

In order capture h_1 , we first need to capture the critical bridge radius H at which polymer relaxation (the right-hand side of equations 25 or 14) becomes negligible in the Newtonian regime ($t < t_1$). H is the bridge radius marking the onset of the coil-stretch transition at which polymer chains start to extend significantly beyond their equilibrium shape, i.e., at which A_{zz} start becoming significantly larger than 1, see §4.1. We already know that $H \rightarrow h_0$ in the limit where the relaxation time τ is so large that polymer relaxation is always negligible in the Newtonian regime, a limit where equation 30 reduces to the classical formula of equation 2. The goal of this subsection is therefore to expand our knowledge to cases where relaxation is not negligible in the Newtonian regime using the Oldroyd-B model.

Figure 10 shows the numerical time evolution of the non-dimensional minimum bridge / filament radius h/h_0 for a fixed Ohnesorge number $Oh = 2.07$, viscosity ratio $S = 0.988$ and $h_0/R_0 = 0.23$ with three Deborah numbers De spanning four orders of magnitude (see equations 5, 6 and 19 for definitions). We only consider the value of A_{zz} at this minimum-radius position along the bridge / filament since this is where polymer chains are the most stretched. This maximum value, simply denoted A_{zz} from now on, is plotted in figure 10 on the right y -axis. Note that all h/h_0 curves are identical in the Newtonian regime, only

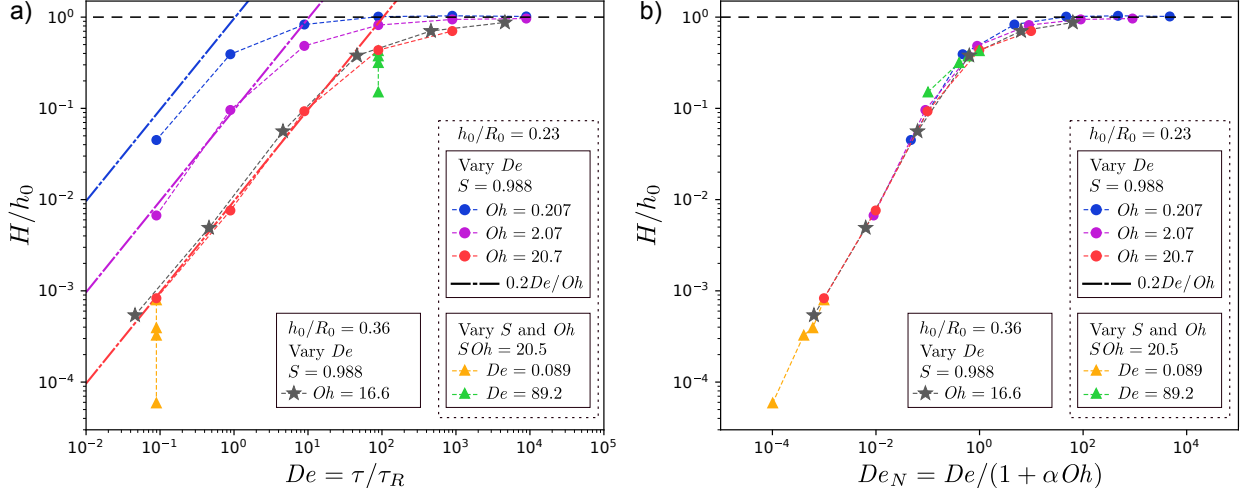


Figure 11: Numerical values of H/h_0 against the Deborah number $De = \tau/\tau_R$ based on the inertio-capillary time scale τ_R (a) and against the general Deborah number $De_N = \tau/\tau_N$ based on the general time scale $\tau_N = \tau_R(1 + \alpha Oh)$ with $\alpha = 4.3$ (b) for various parameters, the same in (a) and (b). Dots (\bullet) correspond to $h_0/R_0 = 0.23$ and $S = 0.988$ with $Oh = 0.207$ (blue) 2.07 (purple) and 20.7 (red) with De ranging between 8.92×10^{-2} and 8.92×10^3 (last De excluded for the largest Oh). Triangles (\blacktriangle) correspond to $h_0/R_0 = 0.23$ with $De = 8.92 \times 10^{-2}$ (yellow) and 8.92×10^1 (green) with varying both S (between 0.1 and 0.988) and Oh while keeping $S Oh$ constant and equal to 9.88. Stars (\star) correspond to $h_0/R_0 = 0.362$ with $Oh = 16.6$ and $S = 0.988$ with De ranging between 4.59×10^{-2} and 8.92×10^3 .

diverging at the transition to the elastic regime at different radii h_1 . The time reference t_c corresponds to the time at which the bridge would break if this transition did not occur. This is highlighted by the fact that the self-similar viscous thinning law of equation 21, which becomes $h/h_0 = 0.0709(t_c - t)/(Oh\tau_R)$ with our choice of non-dimensionalisation and which is plotted in figure 10, fits numerical results close to the transition. Note that simulations could often not be continued long after the transition.

Figure 10 shows how, for a given flow history in the Newtonian regime, polymer chains start stretching at different times depending on the Deborah number. For $De \gg 1$, relaxation is always negligible in the Newtonian regime and A_{zz} therefore increases as $(H/h)^4$ where $H = h_0$, see discussion in §4.1. For $De \ll 1$ however, the flow only becomes strong enough to start stretching polymers (beyond their equilibrium shape) at small bridge radii where the thinning dynamics has become self-similar and, for $Oh \gg 1$, follows equation 21. In that case, $A_{zz} = 1$ for most of the Newtonian regime, only increasing close to the transition to the elastic regime, following $A_{zz} = (H/h)^4$ where $H \ll h_0$ is the characteristic bridge radius at which A_{zz} starts increasing. Values of H are estimated by fitting A_{zz} with $(H/h)^4$, using H as a fitting parameter, see figure 10, as was done in figure 7 for experimental results.

Values of H/h_0 are plotted against the Deborah number in figure 11(a) for Ohnesorge

numbers between 0.2 and 20. The low- De behaviour corresponds to cases where polymers only start stretching within the self-similar thinning regime where the thinning dynamics follows a scaling of the form $h = B(t_c - t)^\beta$ with $B \sim (\gamma/\rho)^{1/3}$ and $\beta = 2/3$ in the inviscid limit ($Oh \ll 1$, see equation 20) and $B \sim \gamma/\eta_0$ and $\beta = 1$ in the viscous limit ($Oh \gg 1$, see equation 21). The coil-stretch transition occurs when the extension rate $\dot{\epsilon} = -2\dot{h}/h \sim 2\beta/(t_c - t)$ becomes of the order of $1/\tau$, i.e., at a time $t_H = t_c - 2\beta\tau$. Therefore, the bridge radius $H = h(t_H)$ marking the onset of the coil-stretch transition scales as

$$H \sim (\gamma\tau^2/\rho)^{1/3} \quad \Leftrightarrow \quad H/h_0 \sim De^{2/3} \quad (33)$$

in the inviscid limit ($Oh \ll 1$), as first derived by Campo-Deaño & Clasen [19], or as

$$H \sim \gamma\tau/\eta_0 \quad \Leftrightarrow \quad H/h_0 \sim De/Oh = \tau/\tau_{\text{visc}} \quad (34)$$

in the viscous limit ($Oh \gg 1$). The scaling of equation 34 is shown in figure 11(a) with a prefactor 0.2 and shows a good agreement with the values of H for the two largest Ohnesorge numbers. Unfortunately, no simulations could be performed for $Oh \ll 1$ to test equation 33. Note that, in this peculiar limit where polymer chains only start stretching within the self-similar thinning regime, H , and therefore h_1 given by equation 30, do not depend on h_0 and are therefore independent of the size of the system, in sharp contrast with the high- De limit where $H = h_0$ and therefore $h_1 \propto h_0^{4/3}$, see equation 2. In fact, inserting equation 33 or 34 into equation 30 gives

$$h_1 \sim (G(\gamma\tau^8/\rho^4)^{1/3})^{1/3} \quad (35)$$

in the inviscid limit ($Oh \ll 1$), or

$$h_1 \sim (G\gamma^3\tau^4/\eta_0^4)^{1/3} \quad (36)$$

in the viscous limit ($Oh \gg 1$).

In the high- De limit, $H/h_0 \rightarrow 1$ since polymer relaxation becomes negligible even at the onset of capillary thinning where $h = h_0$. However, while all curves in figure 11(a) have the same shape, the Deborah number at which H/h_0 reaches 1 depends on the Ohnesorge number. This is because we chose to express the Deborah number as $De = \tau/\tau_R$ where $\tau_R = (\rho h_0^3/\gamma)^{1/2}$ is the inertio-capillary time scale which is not relevant for the moderate to large Ohnesorge number featured in figure 11(a). The relevant time scale for the thinning dynamics at large Oh is $\tau_{\text{visc}} = Oh\tau_R = \eta_0 h_0/\gamma$ and we would hence expect that $H/h_0 = \mathcal{O}(1)$ not when $\tau/\tau_R = \mathcal{O}(1)$ but when $\tau/\tau_{\text{visc}} (= De/Oh) = \mathcal{O}(1)$. In figure 11(b), we show that values of H/h_0 indeed rescale on a single curve when plotted against a generalised Deborah number $De_N = \tau/\tau_N$ where τ_N , defined as

$$\tau_N = \tau_R(1 + \alpha Oh), \quad (37)$$

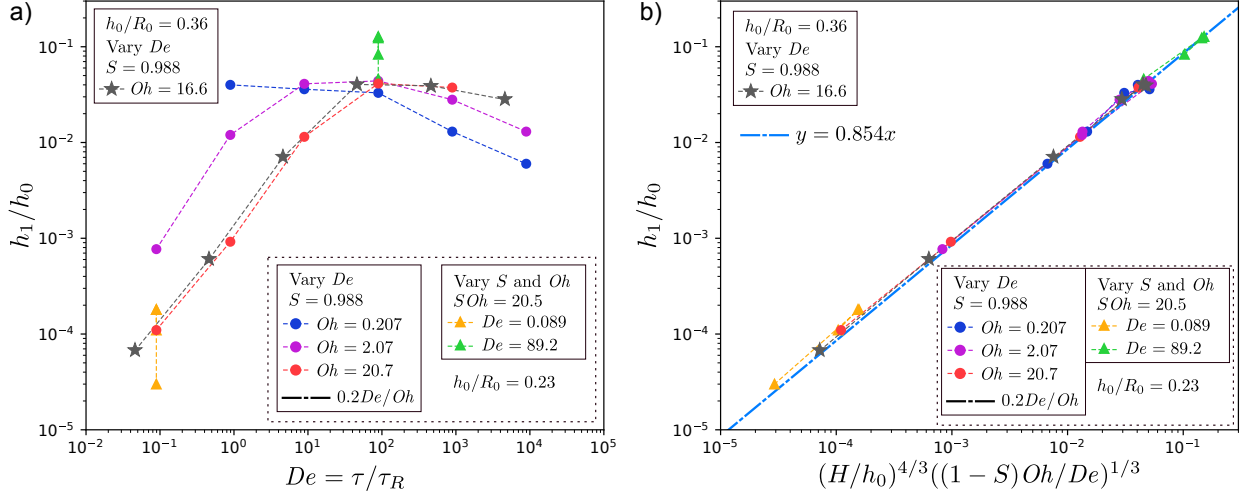


Figure 12: Numerical (non-dimensional) transition radius h_1/h_0 against the Deborah number $De = \tau/\tau_R$ (a) and against $(H/h_0)^{4/3}((1-S)Oh/De)^{1/3}$ (b). The dash-dotted line in (b) is the line of equation $y = 0.854x$. The legend and range of parameters (Oh , De , S and h_0/R_0) are the same as in figure 11.

is an empirical attempt at expressing the general time scale of the thinning dynamics in the Newtonian regime for any Oh , connecting the low and high- Oh scalings τ_R and τ_{visc} , where $\alpha = 4.3$ is a fitting parameter. This scaling ensures that $H/h_0 = \mathcal{O}(1)$ when $De_N = \mathcal{O}(1)$ for any Ohnesorge number. However, according to equations 33 and 34, we expect different scalings for $De_N \ll 1$, namely, $H/h_0 \sim De_N^{2/3}$ for $Oh \ll 1$ and $H/h_0 \sim De_N$ for $Oh \gg 1$.

We have so far varied De and Oh for a fixed viscosity ratio $S = 0.988$ and a fixed droplet volume characterised by a fixed value of $h_0/R_0 = 0.23$. In order to further investigate the generality of the H/h_0 dependence on De_N identified in figure 11(b), we therefore performed additional simulations. Two sets of simulations were performed for $De = 0.089$ and 89.2 respectively, keeping $h_0/R_0 = 0.23$, where both S and Oh were varied while keeping $SOh = \eta_s/\sqrt{\rho\gamma h_0}$ constant and equal to 9.88 . In each case, S is varied between 0.1 and 0.988 where the total (constant shear) viscosity $\eta_0 = \eta_s + \eta_p$ is respectively dominated by the polymer and by the solvent contribution. All these additional data points in figure 11(a) rescale on the same curve identified in figure 11(b). This is because all these cases correspond to $Oh \gg 1$ where $\tau_{\text{visc}} = \eta_0 h_0/\gamma$ is the relevant time scale of the thinning dynamics in the Newtonian regime (and not $\eta_s h_0/\gamma$ for example), regardless of the value of S .

Additionally, a set of simulation was performed for a larger (non-dimensional) droplet volume corresponding to $h_0/R_0 = 0.36$, varying De for a fixed $Oh = 16.6$ and $S = 0.988$. These additional data points in figure 11(a) also rescale on the same curve identified in figure 11(b). This is because h_0 is the relevant time scale of the problem and sets τ_N (see equation 37), in agreement with our experimental results which show that h_1 increases when increasing

the droplet volume for a given plate diameter due to the increase in h_0 (see figure 4(b)).

We can finally test the prediction of equation 30 for the transition radius h_1 between the Newtonian and elastic regime which, in non-dimensional terms, reads

$$\frac{h_1}{h_0} = \left(\frac{H}{h_0}\right)^{4/3} \left[\frac{(1-S)Oh}{pDe}\right]^{1/3}. \quad (38)$$

Figure 12(a) shows that h_1/h_0 , which is estimated from the numerical h/h_0 curves for the same sets of parameters as in figure 11, does not monotonically increase or decrease with De . This is because, at low De (more specifically at low $De_N = \tau/\tau_N$, see figure 11), $H/h_0 \propto De$ for $Oh \gg 1$ according to equation 34, implying that $h_1/h_0 \propto De$ according to equation 38 while, at high $De(N)$, $H/h_0 = 1$, implying that $h_1/h_0 \propto De^{-1/3}$ according to equation 38. We find that all values of h_1/h_0 indeed rescale on a single master curve when plotted against $(H/h_0)^{4/3}((1-S)Oh/De)^{1/3}$ in figure 12(b) where we find that the value of p in equation 38 should be $p \approx 1.6$. Note that the value of p depends on the exact definition of h_1 , since the transition between the Newtonian and elastic regime is not necessarily sharp.

The validation of equation 38 proves that, while equation 2 is valid for a fast plate separation protocol, relaxation of polymer chains must be taken into account to allow for values of $H < h_0$ for a slow plate separation protocol. It also proves that, when interested in the minimum bridge / filament radius and maximum polymer extension at that point, the full 2-dimensional problem can be reduced to the simple force balance equation such as equation 23 (which only strictly applies to a cylindrical thread) without losing predictive power since equation 38 (or, equivalently, equation 30) is based on equation 23.

5. FENE-P prediction for h_1

We now consider how finite extensibility effects, described by the FENE-P model, can affect the transition radius $h_1 = h(t_1)$ at the onset of the elastic regime. We first derive a theoretical model validated by numerical simulations in §5.1 before using it in §5.2 to explain some of the discrepancies observed between the Oldroyd-B theory and experiments.

5.1. Simulations and theory

Figure 13(a) shows how, for a fixed Oh , De , S and h_0/R_0 , decreasing L^2 leads to an increase in h_1 . This can be seen as counter intuitive since a decrease in L^2 implies that chains are shorter and therefore less elastic, which should imply a delayed transition to the elastic regime (smaller h_1). As we discuss in §6, this apparent contradiction is resolved by considering that shorter chains have shorter relaxation times, leading to smaller values of H and therefore of h_1 , which is not taken into account in the simulations of figure 13(a) where Deborah number is kept constant.

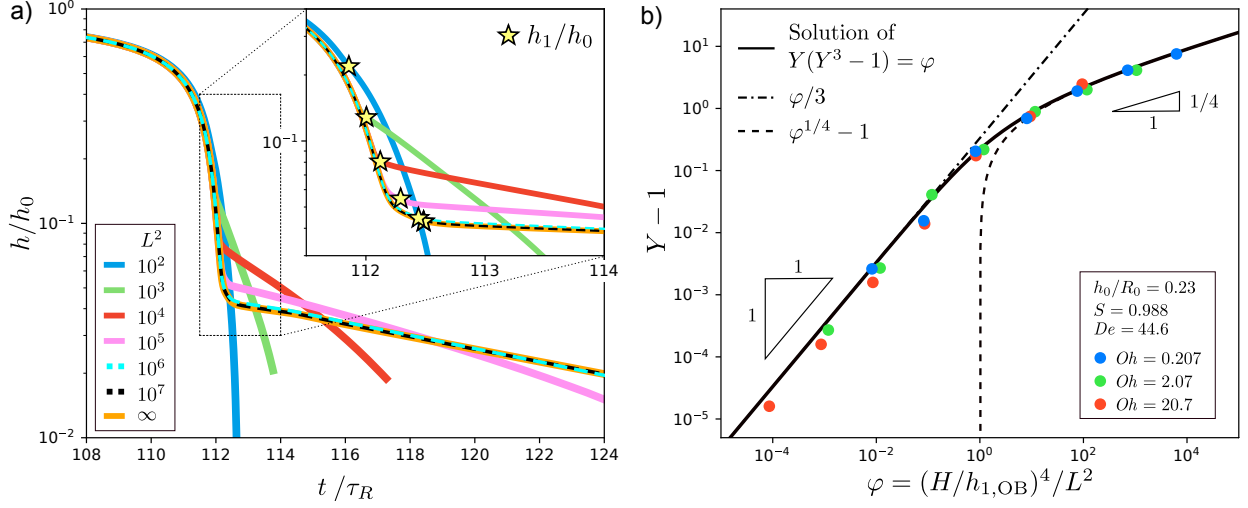


Figure 13: (a) Numerical time evolution of h/h_0 using the FENE-P model with L^2 ranging between 10^2 and 10^7 , as well as $L^2 = +\infty$ (Oldroyd-B limit), for fixed $Oh = 2.07$, $De = 44.6$, $S = 0.988$ and $h_0/R_0 = 0.23$. The inset figure is a zoomed version for a better visualisation of the transition to the elastic regime at $h = h_1$. Simulations start at $t = 0$ used as the time reference. (b) $Y - 1$ against φ (see equation 40) (where $Y = h_1/h_{1,OB}$ where $h_{1,OB}$ is the Oldroyd-B limit of h_1) for L^2 ranging between 10^2 and 10^8 with $Oh = 0.207$, 2.07 and 20.7 and fixed values of $De = 44.6$, $S = 0.988$ and $h_0/R_0 = 0.23$. Values are compared with the analytical solution of equation 40 with limit scalings of equation 42.

Note that in figure 13(a), the thinning rate $|\dot{h}/h|$ in the elastic regime ($t > t_1$) is larger than $1/3\tau$ for the lowest L^2 values while, for the largest L^2 values, the elastic regime initially follows equation 1. This is because polymer chains are already close to being fully extended at the onset of the elastic regime for the lowest L^2 values, as discussed in our previous paper [21] where we explored the possibility to invoke this effect to explain variations of the apparent relaxation time τ_e (see, e.g., figure 3(c,e)).

The reason why h_1 increases as L^2 decreases for a fixed De is because the elastic stress $\sigma_{p,zz} \approx GfA_{zz}$ (assuming $A_{zz} \gg 1$ at the transition, see equation 13) increases faster during the Newtonian regime ($t < t_1$) as L^2 decreases. This is because $f \approx 1/(1 - A_{zz}/L^2)$ (assuming $A_{zz} \gg 1 > A_{rr}$) diverges as A_{zz} approaches L^2 to model the stiffening of polymer chains as they approach full extension. Formally, assuming that the transition occurs when the elastic stress reaches a fraction p of the capillary pressure, i.e., when $\sigma_{p,zz} = p\gamma/h$ (where the $(2X - 1)$ prefactor is integrated in p , see §4.1), we get

$$p \frac{\gamma}{h_1} = G \frac{A_1}{1 - A_1/L^2}, \quad (39)$$

where $h_1 = h(t_1)$ and $A_1 = A_{zz}(t_1)$ are the values at the transition. We assume that the bridge

radius H marking the onset of the coil-stretch transition is unaffected by finite extensibility effects since, at the onset of this coil-stretch transition, A_{zz} is still close to 1 and therefore $f \approx 1$. Assuming that relaxation becomes negligible between the onset of the coil-stretch transition and the onset of the elastic regime, i.e., for $h_1 < h < H$, we use $A_{zz} = (H/h)^4$ (see equation 28) from which we get $A_1 = (H/h_1)^4$. Injecting this scaling in equation 39 leads to a polynomial equation for h_1 in the form

$$h_1 = h_{1,\text{OB}} \times Y(\varphi), \quad Y(Y^3 - 1) = \varphi, \quad \varphi = \frac{A_{1,\text{OB}}}{L^2}, \quad (40)$$

where

$$h_{1,\text{OB}} = \left(\frac{GH^4}{p\gamma} \right)^{1/3} \quad \text{and} \quad A_{1,\text{OB}} = \left(\frac{H}{h_{1,\text{OB}}} \right)^4 \quad (41)$$

are the value of h_1 and A_1 predicted in the Oldroyd-B limit $L^2 = +\infty$ ($\varphi = 0$), see equation 30 for $h_{1,\text{OB}}$. The two limit scalings of equation 40 corresponding to weak ($\varphi \ll 1$) and strong ($\varphi \gg 1$) finite extensibility effects are

$$Y = \begin{cases} 1 + \varphi/3 & \text{for } \varphi \ll 1, \\ \varphi^{1/4} & \text{for } \varphi \gg 1. \end{cases} \quad (42)$$

In the weak limit ($\varphi \ll 1$), polymer chains are still far from full extension at the onset of the elastic regime while, in the strong limit ($\varphi \gg 1$), the transition occurs significantly sooner than the Oldroyd-B prediction due to the fact that polymer chain have almost already reached full extension at the transition. Indeed, in the strong limit, the transition occurs when $A_{zz} = (H/h)^4$ becomes of the order of L^2 , leading to

$$h_1 \sim \frac{H}{L^{1/2}}, \quad (43)$$

which is equivalent to equation 42 for $\varphi \gg 1$.

Values of Y estimated from numerical simulations using the FENE-P model are plotted against φ in figure 13(b) for three different Ohnesorge numbers, varying L^2 between 10^2 and 10^8 in each case while keeping De , S and h_0/R_0 constant, using an extra Oldroyd-B simulation as a reference to get $h_{1,\text{OB}}$. We find that all data points collapse on a single curve corresponding to the solution of equation 40. In particular, no prefactor is required in the $\varphi \gg 1$ limit. Note that we choose to plot $Y - 1$ instead of Y in order to better visualise the $\varphi \ll 1$ regime. Note that the values of H/h_0 , estimated for each simulation like in figure 10, is found not to depend on L^2 and takes values between 1 and 0.36 for the data of figure 13(b). Equation 40 therefore generalises equation 2 to cases where both finite extensibility effects and polymer relaxation effects are not negligible.

5.2. Experiments

Experimentally, cases where both polymer relaxation and finite extensibility effects are expected to play a role correspond to low polymer concentrations c . Indeed, as c decreases, the transition to the elastic regime is delayed (i.e. h_1 decreases, see figures 5(b) and 6(b)) and polymer chains are therefore expected to be increasingly stretched at the onset of the elastic regime, assuming that their relaxation time becomes equal to the Zimm relaxation τ_Z time which is independent of polymer concentration c (see equation 22). Polymer chains should therefore ultimately approach full extension (at the onset of the elastic regime) below a critical concentration c_{low} introduced by Campo-Deaño & Clasen [19]. For $c < c_{\text{low}}$, the elasto-capillary balance leading to the exponential decay of equation 1 is therefore no longer valid since $A_1 \sim L^2$, leading to filaments thinning rates $|\dot{h}/h| > 1/3\tau$, as shown numerically in figure 13(a) and discussed in our previous paper [21]. This would explain why fitting the elastic regime ($t > t_1$) with an exponential leads to apparent relaxation times τ_e that are smaller than τ_Z , as reported in figure 6(a) for aqueous PEO-4M solutions of concentrations $c \leq 10$ ppm. This would also explain why, as discussed in §4.2 (see triangle symbols in figure 9(b)), transition radii h_1 measured for low polymer concentrations cannot be captured by the Oldroyd-B prediction even when replacing values of $\tau_e < \tau_Z$ by τ_Z .

This idea is tested in figure 14 where experimentally measured values of h_1 ($h_{1,\text{exp}}$) are plotted against the FENE-P theoretical prediction $h_{1,\text{th}} = h_{1,\text{OB}} \times Y(\varphi)$ (see equations 40 and 41) for all polymer solutions and initial bridge radii. We choose $L^2 = \infty$ ($Y = 1$) and $\tau = \tau_e$ as model parameters for data points corresponding to the PEO_{aq} (1 and 2, 500 ppm PEO-4M solution in water), PEO_{visc} (1 and 2, 25 ppm PEO-4M solution in a more viscous solvent) and HPAM solutions since we already know from figure 9(b) that these h_1 values are consistent with the Oldroyd-B prediction of equation 30 (we choose $p = 0.27$ to match the prefactor found in figure 9(b)). The experimentally measured values of h_1 corresponding aqueous PEO-4M solutions of various concentrations in figure 14 (orange triangle symbols) are higher than the Oldroyd-B prediction at low concentrations, as we saw in figure 9(b) where replacing values of $\tau_e < \tau_Z$ by τ_Z was found to be insufficient to explain the discrepancy. The blue triangle symbols in figure 14 show that this discrepancy can be rationalised using the FENE-P model where we chose a value of $L^2 = 1 \times 10^4$ sufficiently small to allow for values of Y sufficiently larger than 1 (i.e., polymer chains close to being fully extended at the onset of the elastic regime) to “fill the remaining gap”, while using $\tau = \max(\tau_e, \tau_Z)$ at the model relaxation time.

This value of $L^2 = 1 \times 10^4$ has the same order of magnitude as the value expected from the microscopic formula [40]

$$L^2 = 3 \left[\frac{j \sin^2(\theta/2) M_w}{C_\infty M_u} \right]^{2(1-\nu)}, \quad (44)$$

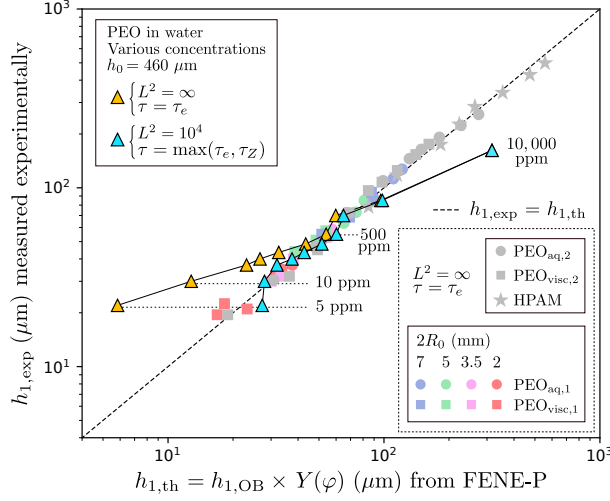


Figure 14: Experimentally measured h_1 values ($h_{1,\text{exp}}$) against FENE-P's theoretical prediction $h_{1,\text{th}} = h_{1,\text{OB}} \times Y(\varphi)$ (see equations 40 and 41) for various polymer solutions and initial bridge radii. Values of the FENE-P model parameters τ and L^2 are indicated in legends (η_p values are the ones from shear rheology). The discrepancy between experiments and the Oldroyd-B prediction for h_1 at low polymer concentration can be rationalised by finite extensibility effects, see main text.

which gives L^2 between 1.6×10^4 and 1.3×10^5 for PEO of molecular weight $M_w = 4 \times 10^6$ g/mol, for solvent quality exponents ν between $3/5$ (good solvent) and $1/2$ (theta solvent), where M_u is the monomer molecular weight, $\theta = 109^\circ$ the C-C bond angle, $j = 3$ the number of bonds of a monomer and $C_\infty = 4.1$ the characteristic ratio [49]. Assuming that ν is between $1/2$ and $3/5$, the discrepancy can be explained by a value M_w less than 4×10^6 g/mol stemming from polymer degradation during mixing when preparing the stock solution. Note that choosing $L^2 = 1 \times 10^4$ leads to values of Y close to 1 (up to 1.18) for the PEO_{aq} (1 and 2), PEO_{visc} (1 and 2) and HPAM solutions, consistent with the agreement between experiments and the Oldroyd-B theory for these solutions in figure 14, as shown by the small difference between the $L^2 = \infty$ (orange) and $L^2 = 1 \times 10^4$ (blue) triangle symbols for $c = 500$ ppm which corresponds to the PEO_{aq,1} solution.

6. Conclusions and discussions

We have shown experimentally that the classical formula of equation 2 for the bridge / filament radius h_1 marking the onset of the elastic regime does not hold for slow filament thinning techniques such as CaBER with a slow plate separation protocol. This is because, unlike what is assumed to derive equation 2, polymer chains do not necessarily start stretching (beyond their equilibrium coiled configuration) at the threshold of the Rayleigh-Plateau

instability (with minimum bridge radius h_0), but only do so when the bridge thinning rate becomes comparable to the inverse of their relaxation time. This was confirmed numerically using the Oldroyd-B model where we have shown that, in the low-relaxation-time limit where polymer chains only start stretching when the bridge thinning dynamics has become self-similar, h_1 does not depend on h_0 anymore, as anticipated by Campo-Deaño & Clasen [19]. Our generalised formula (see equation 30 or 38) is in principle valid for any pinch-off experiment, e.g., in dripping experiments, provided that polymer chains are relaxed at the onset of capillary thinning (no pre-stress).

This formula was extended to finitely extensible polymer chains using a FENE-P description, which solved the observed discrepancy between the Oldroyd-B theory and values of h_1 measured for low polymer concentrations. This is consistent with the fact that apparent relaxation times τ_e less than the Zimm relaxation times were measured at these low concentrations, an anomaly also reported by Campo-Deaño & Clasen [19] which stems from polymer chains being close to full extension at the onset of the elastic regime, a case where equation 1 is no longer valid and thinning rates $|\dot{h}/h| > 1/3\tau$ are observed, as we discuss in our previous paper [21].

Our generalised Oldroyd-B formula of equation 30 solves an apparent paradox of equation 2 which predicts that the transition to the elastic regime occurs sooner as polymer chains get shorter for a fixed (mass) concentration. Indeed, equation 2 predicts $h_1 \propto G^{1/3}$ where the elastic modulus scales with molecular weight as $G \propto M_w^{-1}$ in the Rouse-Zimm theory [40], yielding $h_1 \propto M_w^{-1/3}$ which increases as M_w decreases. This is counter intuitive since shorter chains should imply lower elasticity and therefore a delayed transition, h_1 approaching 0 as polymer chains approach monomer size. This apparent paradox is solved by realising that shorter chains have a shorter (Zimm) relaxation time since $\tau_Z \propto M_w^{3\nu}$ [40], where ν is the solvent quality exponent, implying that H (see equation 30) should start decreasing as M_w decreases for sufficiently low Deborah numbers (see figure 11). In the low-relaxation-time (equivalently low- M_w) limit where polymer chains only start stretching when the bridge thinning dynamics has become self-similar, we get $h_1 \propto M_w^{(8\nu-1)/3}$ for $Oh \ll 1$ and $h_1 \propto M_w^{(12\nu-1)/3}$ for $Oh \gg 1$ according to equations 35 and 36, both exponents being positive for any ν between 1/2 (theta solvent) and 3/5 (good solvent). This remains true even in the limit where polymer chains are almost fully extended at the onset of the elastic regime since equation 43 predicts $h_1 \propto M_w^{(5\nu-1)/2}$ for $Oh \ll 1$ and $h_1 \propto M_w^{(7\nu-1)/2}$ for $Oh \gg 1$ according to equations 33 and 34 for H , using $L \propto M_w^{1-\nu}$ (see equation 44).

We saw in §4.2 that experimental values of h_1 can only be rationalised using the apparent (h_0 -dependent) relaxation time τ_e as ‘the’ relaxation time, in contradiction with the idea discussed in our previous paper [21] that the ‘real’ relaxation time should be high- h_0 limit value τ_m . Indeed, when choosing τ_m , equation 30 only works for the PEO_{visc} solution, i.e., the most dilute one in the most viscous solvent. This would suggest that τ_e is the ‘true’

relaxation time, and not τ_m . This implies that a given polymer solution should exhibit the same thinning rate regardless of the system size (plate diameter or droplet volume), inconsistent with our observations of a system-size dependent apparent relaxation time τ_e (see figure 3(c,e)). Therefore, if τ_e really measures the ‘true’ relaxation, it implies that some rheological property of a polymer solution somehow ‘changes’ when being tested with a different plate diameter via a mechanism which we could not identify and which is unlikely to be evaporation or polymer degradation, as we discussed in our previous paper [21]. Another possibility is that the solution in fact does not change, meaning that the system-size dependence of τ_e is *not* an artefact, in which case it would be only by coincidence that we could successfully capture experimental values of h_1 using τ_e . This would imply that the Oldroyd-B and FENE-P models miss some important features of polymer dynamics in extensional flows, strengthening the already established need for better constitutive equations. Future works will determine if more sophisticated models such as Conformation-Dependent Drag (CDD) models, accounting for the action of both chain stretching and intermolecular hydrodynamic interactions on the friction coefficient [43, 50], are able to rationalise our experimental results on the system-size dependence of both τ_e and h_1 .

Conflicts of interest The authors declare no conflicts of interest.

Funding M. A. Herrada acknowledges funding from the Spanish Ministry of Economy, Industry and Competitiveness under Grant PID2022-140951O.

References

- [1] A. Gaillard, R. Sijs, D. Bonn, What determines the drop size in sprays of polymer solutions?, *Journal of Non-Newtonian Fluid Mechanics* 305 (2022) 104813.
- [2] B. Keshavarz, V. Sharma, E. C. Houze, M. R. Koerner, J. R. Moore, P. M. Cotts, P. Threlfall-Holmes, G. H. McKinley, Studying the effects of elongational properties on atomization of weakly viscoelastic solutions using rayleigh ohnesorge jetting extensional rheometry (rojer), *Journal of Non-Newtonian Fluid Mechanics* 222 (2015) 171–189.
- [3] B. Keshavarz, E. C. Houze, J. R. Moore, M. R. Koerner, G. H. McKinley, Ligament mediated fragmentation of viscoelastic liquids, *Physical review letters* 117 (15) (2016) 154502.
- [4] U. Sen, C. Datt, T. Segers, H. Wijshoff, J. H. Snoeijer, M. Versluis, D. Lohse, The retraction of jetted slender viscoelastic liquid filaments, *Journal of fluid mechanics* 929 (2021) A25.
- [5] Y. Christanti, L. M. Walker, Effect of fluid relaxation time of dilute polymer solutions on jet breakup due to a forced disturbance, *Journal of Rheology* 46 (3) (2002) 733–748.

- [6] B. Scharfman, A. Techet, J. Bush, L. Bourouiba, Visualization of sneeze ejecta: steps of fluid fragmentation leading to respiratory droplets, *Experiments in Fluids* 57 (2) (2016) 1–9.
- [7] B. T. Gidreta, H. Kim, Effects of physical property changes of expelled respiratory liquid on atomization morphology, *Journal of Fluid Mechanics* 960 (2023) A10.
- [8] A. Bazilevsky, V. Entov, M. Lerner, A. Rozhkov, Failure of polymer solution filaments, *Polymer Science Series ac/c of Vysokomolekuliarnye Soedineniia* 39 (1997) 316–324.
- [9] S. L. Anna, G. H. McKinley, Elasto-capillary thinning and breakup of model elastic liquids, *Journal of Rheology* 45 (1) (2001) 115–138.
- [10] M. Stelter, G. Brenn, A. Yarin, R. Singh, F. Durst, Validation and application of a novel elongational device for polymer solutions, *Journal of Rheology* 44 (3) (2000) 595–616.
- [11] Y. Amarouchene, D. Bonn, J. Meunier, H. Kellay, Inhibition of the finite-time singularity during droplet fission of a polymeric fluid, *Phys. Rev. Lett.* 86 (2001) 3558–3561. doi:10.1103/PhysRevLett.86.3558.
URL <https://link.aps.org/doi/10.1103/PhysRevLett.86.3558>
- [12] V. Tirtaatmadja, G. H. McKinley, J. J. Cooper-White, Drop formation and breakup of low viscosity elastic fluids: Effects of molecular weight and concentration, *Physics of fluids* 18 (4) (2006) 043101.
- [13] S. Rajesh, V. Thiévenaz, A. Sauret, Transition to the viscoelastic regime in the thinning of polymer solutions, *Soft Matter* 18 (16) (2022) 3147–3156.
- [14] J. Dinic, L. N. Jimenez, V. Sharma, Pinch-off dynamics and dripping-onto-substrate (dos) rheometry of complex fluids, *Lab on a Chip* 17 (3) (2017) 460–473.
- [15] V. M. Entov, E. J. Hinch, Effect of a spectrum of relaxation times on the capillary thinning of a filament of elastic liquid, *Journal of Non-Newtonian Fluid Mechanics* 72 (1) (1997) 31–53.
- [16] C. Clasen, J. Eggers, M. A. Fontelos, J. Li, G. H. McKinley, The beads-on-string structure of viscoelastic threads, *Journal of Fluid Mechanics* 556 (2006) 283–308.
- [17] E. Miller, C. Clasen, J. P. Rothstein, The effect of step-stretch parameters on capillary breakup extensional rheology (CaBER) measurements, *Rheologica acta* 48 (2009) 625–639.
- [18] L. E. Rodd, T. P. Scott, J. J. Cooper-White, G. H. McKinley, Capillary break-up rheometry of low-viscosity elastic fluids, *Applied Rheology* 15 (1) (2005) 12–27.
- [19] L. Campo-Deano, C. Clasen, The slow retraction method (SRM) for the determination of ultra-short relaxation times in capillary breakup extensional rheometry experiments, *Journal of Non-Newtonian Fluid Mechanics* 165 (23-24) (2010) 1688–1699.

- [20] C. Wagner, Y. Amarouchene, D. Bonn, J. Eggers, Droplet detachment and satellite bead formation in viscoelastic fluids, *Physical review letters* 95 (16) (2005) 164504.
- [21] A. Gaillard, M. A. H. Gutierrez, A. Deblais, J. Eggers, D. Bonn, Beware of CaBER: filament thinning rheometry doesn't give 'the' relaxation time of polymer solutions, arXiv preprint arXiv:2309.08440 (2023).
- [22] L. Casanellas, M. A. Alves, R. J. Poole, S. Lerouge, A. Lindner, The stabilizing effect of shear thinning on the onset of purely elastic instabilities in serpentine microflows, *Soft matter* 12 (29) (2016) 6167–6175.
- [23] C. W. Macosko, *Rheology: principles, measurements, and applications*, Wiley-vch, 1994.
- [24] W. W. Graessley, Polymer chain dimensions and the dependence of viscoelastic properties on concentration, molecular weight and solvent power, *Polymer* 21 (3) (1980) 258–262.
- [25] L. A. Slobozhanin, J. M. Perales, Stability of liquid bridges between equal disks in an axial gravity field, *Physics of Fluids A: Fluid Dynamics* 5 (6) (1993) 1305–1314.
- [26] J. H. Snoeijer, A. Pandey, M. A. Herrada, J. Eggers, The relationship between viscoelasticity and elasticity, *Proc. R. Soc. A* 476 (2020) 20200419.
- [27] M. Herrada, J. M. Montanero, A numerical method to study the dynamics of capillary fluid systems, *Journal of Computational Physics* 306 (2016) 137–147.
- [28] R. Sattler, C. Wagner, J. Eggers, Blistering pattern and formation of nanofibers in capillary thinning of polymer solutions, *Physical review letters* 100 (16) (2008) 164502.
- [29] R. Sattler, S. Gier, J. Eggers, C. Wagner, The final stages of capillary break-up of polymer solutions, *Physics of Fluids* 24 (2) (2012) 023101.
- [30] J. Eggers, Instability of a polymeric thread, *Physics of Fluids* 26 (3) (2014) 033106.
- [31] A. V. Semakov, V. G. Kulichikhin, A. K. Tereshin, S. V. Antonov, A. Y. Malkin, On the nature of phase separation of polymer solutions at high extension rates, *Journal of Polymer Science Part B: Polymer Physics* 53 (8) (2015) 559–565.
- [32] A. Deblais, M. Herrada, I. Hauner, K. P. Velikov, T. Van Roon, H. Kellay, J. Eggers, D. Bonn, Viscous effects on inertial drop formation, *Physical review letters* 121 (25) (2018) 254501.
- [33] D. T. Papageorgiou, On the breakup of viscous liquid threads, *Physics of fluids* 7 (7) (1995) 1529–1544.
- [34] G. H. McKinley, A. Tripathi, How to extract the newtonian viscosity from capillary breakup measurements in a filament rheometer, *Journal of Rheology* 44 (3) (2000) 653–670.

- [35] J. Eggers, Universal pinching of 3d axisymmetric free-surface flow, *Physical Review Letters* 71 (21) (1993) 3458.
- [36] J. Eggers, Nonlinear dynamics and breakup of free-surface flows, *Reviews of modern physics* 69 (3) (1997) 865.
- [37] J. Dinic, V. Sharma, Macromolecular relaxation, strain, and extensibility determine elasto-capillary thinning and extensional viscosity of polymer solutions, *Proceedings of the National Academy of Sciences* 116 (18) (2019) 8766–8774.
- [38] M. Stelter, G. Brenn, A. L. Yarin, R. P. Singh, F. Durst, Investigation of the elongational behavior of polymer solutions by means of an elongational rheometer, *Journal of Rheology* 46 (2) (2002) 507–527.
- [39] A. Zell, S. Gier, S. Rafai, C. Wagner, Is there a relation between the relaxation time measured in CaBER experiments and the first normal stress coefficient?, *Journal of Non-Newtonian Fluid Mechanics* 165 (19) (2010) 1265–1274.
- [40] C. Clasen, J. P. Plog, W.-M. Kulicke, M. Owens, C. Macosko, L. E. Scriven, M. Verani, G. H. McKinley, How dilute are dilute solutions in extensional flows?, *Journal of Rheology* 50 (6) (2006) 849–881.
- [41] D. E. Smith, H. P. Babcock, S. Chu, Single-polymer dynamics in steady shear flow, *Science* 283 (5408) (1999) 1724–1727.
- [42] N. Phan-Thien, O. Manero, L. Leal, A study of conformation-dependent friction in a dumbbell model for dilute solutions, *Rheologica acta* 23 (1984) 151–162.
- [43] R. Prabhakar, S. Gadkari, T. Gopesh, M. Shaw, Influence of stretching induced self-concentration and self-dilution on coil-stretch hysteresis and capillary thinning of unentangled polymer solutions, *Journal of Rheology* 60 (3) (2016) 345–366.
- [44] J. Eggers, M. A. Herrada, J. Snoeijer, Self-similar breakup of polymeric threads as described by the Oldroyd-B model, *Journal of fluid mechanics* 887 (2020) A19.
- [45] C. Wagner, L. Bourouiba, G. H. McKinley, An analytic solution for capillary thinning and breakup of FENE-P fluids, *Journal of Non-Newtonian Fluid Mechanics* 218 (2015) 53–61.
- [46] C. Clasen, J. Bico, V. M. Entov, G. H. McKinley, Gobbling drops: the jetting–dripping transition in flows of polymer solutions, *Journal of fluid mechanics* 636 (2009) 5–40.
- [47] F. Ingremeau, H. Kellay, Stretching polymers in droplet-pinch-off experiments, *Physical Review X* 3 (4) (2013) 041002.

- [48] A. Bazilevsky, V. Entov, A. Rozhkov, Breakup of an Oldroyd liquid bridge as a method for testing the rheological properties of polymer solutions, Polymer Science Series AC/C of Vysokomolekuliarnye Soedineniia 43 (7) (2001) 716–726.
- [49] J. Brandrup, E. H. Immergut, E. A. Grulke, A. Abe, D. R. Bloch, Polymer handbook, Vol. 7, Wiley New York etc, 1989.
- [50] R. Prabhakar, C. Sasmal, D. A. Nguyen, T. Sridhar, J. R. Prakash, Effect of stretching-induced changes in hydrodynamic screening on coil-stretch hysteresis of unentangled polymer solutions, Physical Review Fluids 2 (1) (2017) 011301.